Evolution, distribution, and characteristics of rifting in southern Ethiopia

Melody Philippon, Giacomo Corti, Federico Sani, Marco Bonini, Maria-Laura Balestrieri, Paola Molin, Ernst Willingshofer, Dimitrios Sokoutis, Sierd Cloetingh

AGU PUBLICATIONS

Tectonics

RESEARCH ARTICLE
10.1002/2013TC003430

Key Points:
- Rift in southern Ethiopia is investigated through fieldwork and radiometric dating
- Deformation initiates at 10-12 Ma and post 30 ka faulting is evidenced
- Preexisting basement fabrics control the geometry of major border faults

Supporting Information:
- Readme
- Text S1
- Supplemental Figures S1–S2

Correspondence to:
M. Philippon,
melodie.philippon@gm.univ-montp2.fr

Citation:
Philippon, M., G. Corti, F. Sani, M. Bonini, M.-L. Balestrieri, P. Molin, E. Willingshofer, D. Sokoutis, and S. Cloetingh (2014), Evolution, distribution, and characteristics of rifting in southern Ethiopia, *Tectonics*, *33*, 485-508, doi:10.1002/2013TC003430.

Received 29 AUG 2013
Accepted 24 FEB 2014
Accepted article online 3 Mar 2014
Published online 15 APR 2014

Evolution, distribution, and characteristics of rifting in southern Ethiopia

Melody Philippon[1,2], Giacomo Corti[3], Federico Sani[4], Marco Bonini[3], Maria-Laura Balestrieri[3], Paola Molin[5], Ernst Willingshofer[1], Dimitrios Sokoutis[1,6], and Sierd Cloetingh[1]

[1]Faculty of Earth Science, Utrecht University, Utrecht, Netherlands, [2]Gesociences Montpellier, Université de Montpellier 2, UMR CNRS 5243, Montpellier CEDEX 5, France, [3]Istituto di Geoscienze e Georisorse, Consiglio Nazionale delle Ricerche, Florence, Italy, [4]Dipartimento di Scienze della Terra, Università degli Studi di Firenze, Florence, Italy, [5]Dipartimento di Scienze, Università degli Studi di RomaTre, Roma, Italy, [6]Department of Geosciences, University of Oslo, Oslo, Norway

Abstract Southern Ethiopia is a key region to understand the evolution of the East African rift system, since it is the area of interaction between the main Ethiopian rift (MER) and the Kenyan rift. However, geological data constraining rift evolution in this remote area are still relatively sparse. In this study the timing, distribution, and style of rifting in southern Ethiopia are constrained by new structural, geochronological, and geomorphological data. The border faults in the area are roughly parallel to preexisting basement fabrics and are progressively more oblique with respect to the regional Nubia–Somalia motion proceeding southward. Kinematic indicators along these faults are mainly dip slip, pointing to a progressive rotation of the computed direction of extension toward the south. Radiocarbon data indicate post 30 ka faulting at both western and eastern margins of the MER with limited axial deformation. Similarly, geomorphological data suggest recent fault activity along the western margins of the basins composing the Gofa Province and in the Chew Bahir basin. This supports that interaction between the MER and the Kenyan rift in southern Ethiopia occurs in a 200 km wide zone of ongoing deformation. Fault-related exhumation at ~10–12 Ma in the Gofa Province, as constrained by new apatite fission track data, occurred later than the ~20 Ma basement exhumation of the Chew Bahir basin, thus pointing to a northward propagation of the Kenyan rift-related extension in the area.

1. Introduction

Rifting of the continental lithosphere is a major geodynamic process representing a prequel to plate drifting and formation of oceanic basins. Our understanding of rift mechanics comes from the structural, kinematic, geophysical, and geochronological analyses of active continental rifts and passive margins that have shed light on some of the main parameters controlling extensional processes. Primarily, the state of the lithosphere subjected to far field extensional stresses, in terms of thermal structure and crustal thickness, controls both the rift mode and subsidence [*Buck*, 1991, 2004]. Moreover, recent observations from both passive margins [e.g., *White et al*., 2008] and continental rifts [e.g., *Thybo and Nielsen*, 2009; *Keir et al*., 2013] indicate that large volumes of magma can intrude the extending lithosphere during rifting, suggesting that magmatism plays a major role during continental rifting and breakup. Many other studies have highlighted that past tectonic processes, leading to thinning (rifts) or thickening (orogenic wedges and suture zones) of tectonic plates, have induced regional lithospheric-scale heterogeneities that are able to control subsequent rift localization and propagation at both the local and regional scales [e.g., *Ziegler and Cloetingh*, 2004, and references therein].

The East African rift system (EARS) is the ideal place to analyze the characteristics and evolution of rifting, since along its length, it records the progressive narrowing and focusing of the tectonic and volcanic activity at the rift axis, a process that may ultimately lead to continental breakup and subsequent oceanic spreading [e.g., *Ebinger*, 2005]. Within the EARS, the main Ethiopian rift (MER) is of special interest because it connects early continental rifting to the south to incipient seafloor spreading in the Afar depression in the interaction zone between the oceanic basins of the Red Sea and the Gulf of Aden to the north (Figure 1). This rift records polyphase extension reflecting the aforementioned narrowing and focusing of the tectonic and volcanic activity toward the rift axis with time. In particular, the evolution of the rift is characterized by (1) the Miocene development of large border faults, accommodating extension and defining a subsiding rift valley, and (2) a

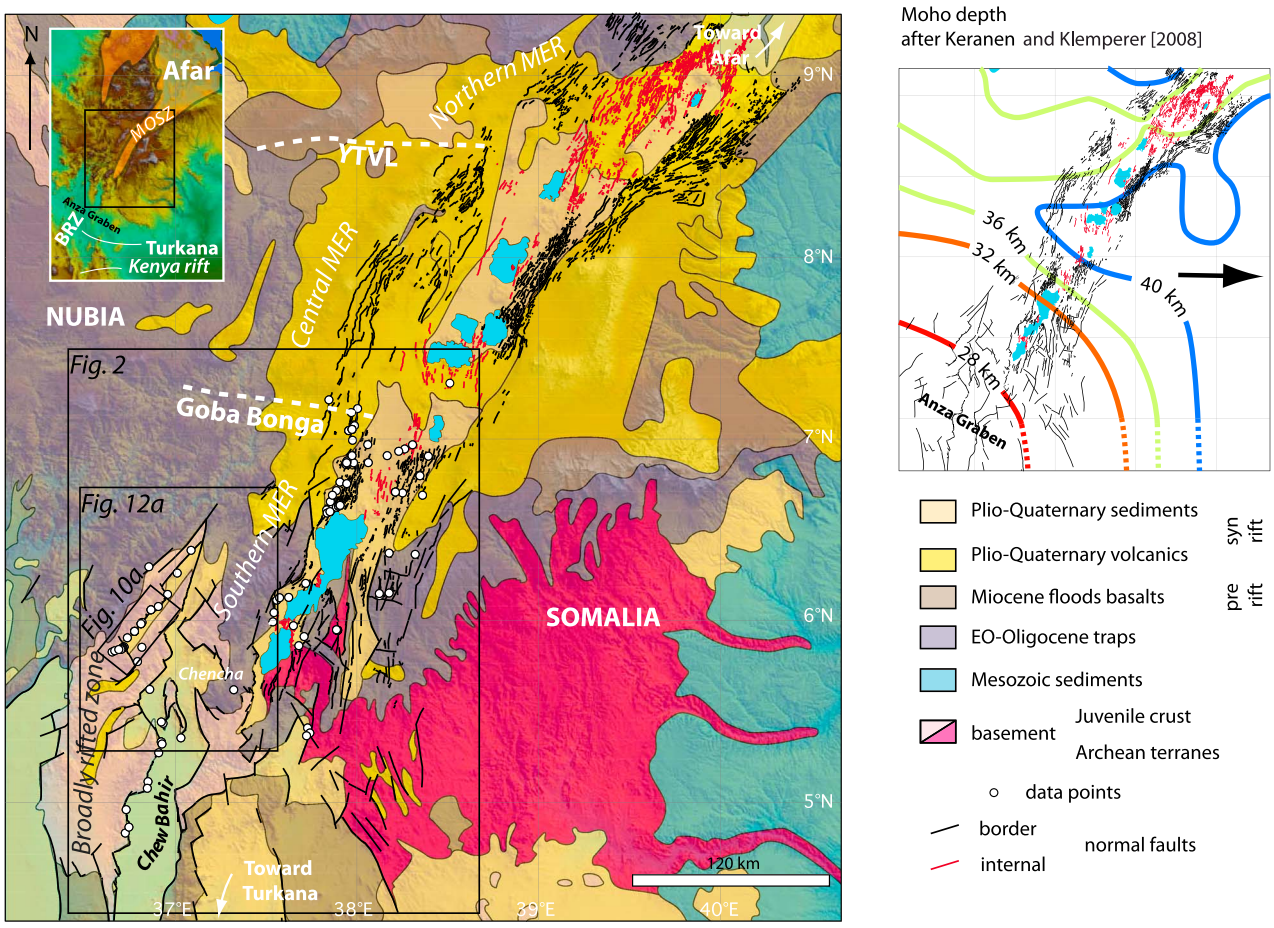

Figure 1. Structural map of the main Ethiopian rift showing the main lithological units (after the geological map of Ethiopia [*Mengesha et al.*, 1996]) and major faults [after *Ebinger et al.*, 2000; *Agostini et al.*, 2011] superimposed onto the SRTM (Shuttle Radar Topography Mission) 90 m digital elevation model. The two main E-W lineaments, the Yerer-Tullu Wellel volcanotectonic lineament and the Goba-Bonga are indicated by dashed white lines. White dots indicate the structural and geochronological data acquired during the field survey. (top left inset) A DEM showing the regional location of the MER, which extends from the Afar to the north to the Turkana to the south, where it merges with the Kenyan rift in the broadly rifted zone, the localization of the Mozambic Ocean suture zone after *Kazmin et al.* [1978]. (right inset) The rift fault pattern and the Moho thickness contours from *Keranen and Klemperer* [2008]. The black arrow in the inset indicates the direction of the bulk regional E-W direction of extension [*Fernandes et al.*, 2004; *Stamps et al.*, 2008; *Kogan et al.*, 2012].

Pliocene to Quaternary migration of the volcanotectonic activity toward the rift floor itself [e.g., *Hayward and Ebinger*, 1996; *Corti*, 2009, and references therein]. This rift evolution is well expressed at the northern termination of the MER, where rifting is believed to be in a mature stage, whereas to the south, rifting becomes less evolved, and the axial deformation becomes less pronounced [e.g., *Hayward and Ebinger*, 1996; *Agostini et al.*, 2011]. Moreover, extensional structures in south Ethiopia become more complex, as they reflect the interaction between the MER and the Kenyan rift that overlap in a 300 km wide system of extensional basins (broadly rifted zone (BRZ)) [e.g., *Ebinger et al.*, 2000] (Figure 1). Timing, style, and kinematics of the volcanotectonic activity are well documented in the northern part and central part of the MER [e.g., *Wolfenden et al.*, 2004; *Agostini et al.*, 2011], but detailed geological, structural data are still relatively sparse in the southern MER and the BRZ of southern Ethiopia [*Ebinger et al.*, 2000].

This study provides new structural (fault kinematics), geochronological (^{14}C dating of faulted debris and apatite fission tracks), and geomorphological (fault scarps plus slope-area analysis) data to constrain the timing, distribution, and characteristics of extensional deformation in southern Ethiopia. These new data are of primary importance since they also provide new insights into the interaction between the Ethiopian and Kenyan rifts in the overlapping area and constraining the relationships between inherited structures and rift development.

2. Tectonic Setting

The MER forms the incipient plate boundary between Nubia and Somalia, whose relative motion is ~95°N–100° E at rates of ~4–6 mm/yr [e.g., *Fernandes et al*., 2004; *Stamps et al*., 2008; *Kogan et al*., 2012]. It extends for about 500 km from the southern edge of the Afar depression in the north to the Turkana depression in the south, where it interacts with the N-S trending Kenyan rift (Figure 1) [*Ebinger et al*., 2000]. The rift is composed of three main segments (northern, central, and southern MER, hereafter referred to as nMER, cMER, and sMER, respectively). These segments are separated by roughly E-W trending transverse structures, namely, the Yerer-Tullu Wellel volcanotectonic lineament [*Abebe et al*., 1998] between the nMER and the cMER and the Goba-Bonga lineament [*Abbate and Sagri*, 1980] separating the cMER from the sMER. Both are characterized by the alignment of normal faults and major volcanoes.

The different MER segments are bounded by major Miocene border faults, which form the main escarpments separating the ~100 km wide rift valley from the surrounding plateaus [e.g., *Boccaletti et al*., 1998] (Figure 1). In the nMER, the large offset border faults have been deactivated during the late Pliocene-Quaternary, and recent deformation has shifted to axial tectonomagmatic segments, where significant magmatic modification of the crust and lithosphere has been imaged [e.g., *Bastow et al*., 2011]. This could be interpreted as an evolutionary step from continental rifting toward early breakup stage, with the axial tectonomagmatic segments representing incipient mid-ocean spreading centers [e.g., *Keranen et al*., 2004]. To the south, less pronounced axial deformation, more limited (or absent) magmatic modification of the crust and lithosphere, and the activity of the border faults point to a less evolved rifting stage [e.g., *Hayward and Ebinger*, 1996].

In particular, in the sMER, large offset border faults produce impressive escarpments such as the Chencha escarpment that bound the rift valley [e.g., *Hayward and Ebinger*, 1996]. Although the sMER has been affected by an early Miocene deformation phase related to the northern propagation of the Kenyan rift, a significant slip on border faults occurred only during the Pliocene [*Bonini et al*., 2005]. The axial deformation is practically negligible in this sector of the MER [*Hayward and Ebinger*, 1996; *Agostini et al*., 2011]. Similarly, volcanic activity in the sMER is much more limited than in the cMER and nMER; specifically, areas of Quaternary-recent volcanic activity are restricted to the rift margins (e.g., north Lake Abaya), or limited portions of the rift floor (e.g., the land bridge—Bridge of God—separating Lake Abaya from Lake Chamo [*Ebinger et al*., 1993]). The southern termination of the MER occurs within the BRZ, the complex region of interaction with the Kenyan rift where the extensional deformation widens up to 200–300 km [*Ebinger et al*., 2000] (Figure 2). In particular, this area is composed of a series of subparallel extensional basins that, to the west of the sMER, give rise to the so-called Gofa Province [*Moore and Davidson*, 1978]. To the south, the continuation of the Gofa Province is represented by the Chew Bahir basin, which trends roughly N-S although characterized by highly segmented border faults (Figure 2).

Active extensional deformation in southern Ethiopia is testified by diffuse seismic activity [e.g., *Gouin*, 1979], with historical earthquakes up to magnitude 6.3 [*Asfaw*, 1990; *Ayele and Arvidsson*, 1998]. Seismic activity encompasses a wide area, with events affecting the sMER, the Gofa Province, and the Chew Bahir basin (Figure 2). A major seismic sequence occurred in this area during the mid-1980s, with one event during 1985 (20 August, $M_w = 5.3$) and three major earthquakes during 1987 (7 October, $M_w = 5.1$; 25 October, $M_w = 6.3$; and 28 October, $M_w = 5.9$). These events were characterized by shallow focal depth (<15 km) and normal faulting mechanisms [*Ayele and Arvidsson*, 1998]. Surface fracturing associated with these earthquakes [*Asfaw*, 1990; *Ayele and Arvidsson*, 1998] has been related to slip along main border faults [e.g., *Ebinger et al*., 2000].

The East African lithosphere contains several inherited structures that differ in both age and scale. The oldest one is the NE-SW trending Mozambique Ocean suture zone (MOSZ), which puts in contact the 870 Ma Neoproterozoic juvenile crust to the west with the 2 Ga Archean basement to the east [*Kazmin et al*., 1978; *Stern*, 1994, 2002] (Figure 1). Ophiolites belonging to this suture zone have been dated between 880 and 690 Ma [*Kroner et al*., 1992; *Claesson et al*., 1984; *Pallister et al*., 1988]. The regional NNE-SSW trending foliation, observed in the basement, results from the continental collision related to the closure of the Mozambic Ocean and the accretion of East Gondwana to West Gondwana [*Kazmin et al*., 1978; *Stern*, 1994, 2002].

During the Mesozoic, and until the Cenozoic, East Africa has been affected by a series of NW-SE trending grabens [e.g., *Guiraud et al*., 2005], related to significant crustal thinning, which introduced further prerift heterogeneities. The largest heterogeneity is the NW-SE striking Anza graben of southern Ethiopia that is

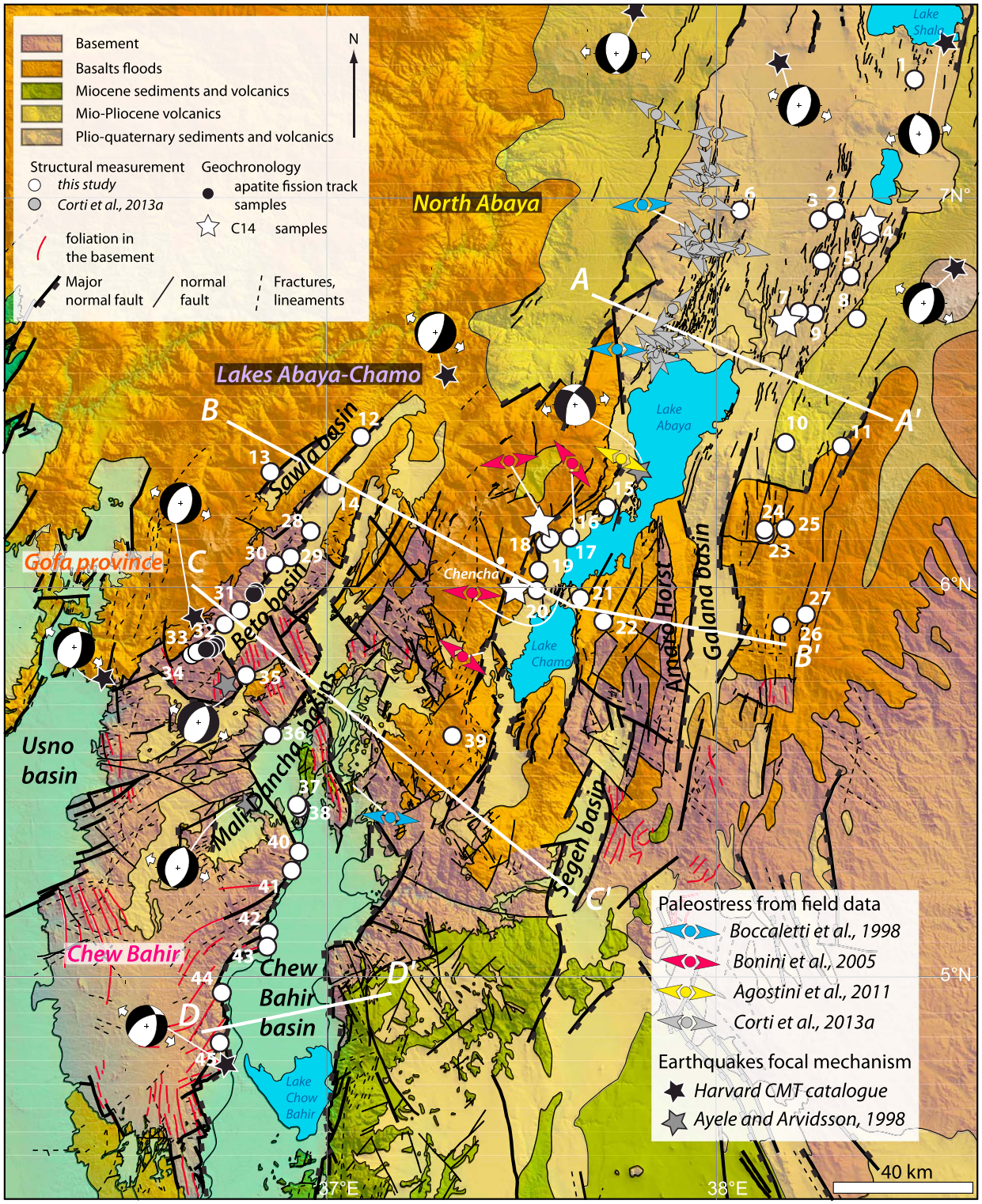

Figure 2. Simplified geological map of southern Ethiopia (after [*Davidson*, 1983]; geological map of Ethiopia [*Mengesha et al.*, 1996]). Major faults and basement fabrics [after *Ebinger et al.*, 2000; this work] are superimposed onto the SRTM digital elevation model. White lines indicate the trace of the four cross sections (AA', BB', CC', and DD') illustrated in Figures 4–7. White dots indicate the sites of structural measurements. White stars correspond to the location of ^{14}C dating samples. Black dots show the location of basement samples for apatite fission track analysis. Fault kinematics in southern Ethiopia is shown as black and gray stars indicating earthquake locations and focal mechanisms from Harvard CMT catalog, *Foster and Jackson* [1998], and *Ayele and Arvidsson* [1998], respectively. The blue, red, yellow, and gray arrows indicate the direction of extension obtained from paleostress analysis from the following previous works: *Boccaletti et al.* [1998], *Bonini et al.* [2005], *Agostini et al.* [2011], and *Corti et al.* [2013a].

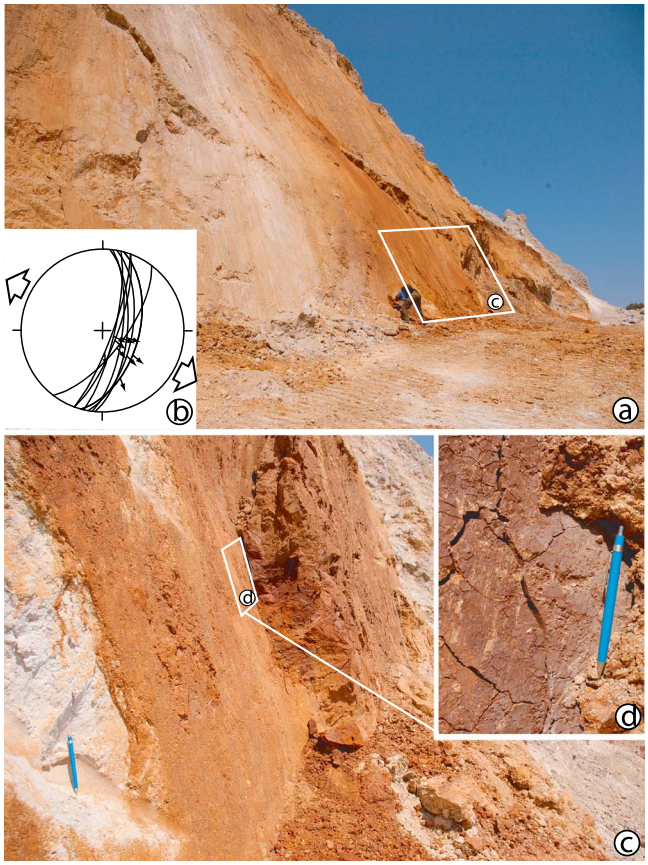

Figure 3. Site 4, where fault debris suitable for ^{14}C dating has been sampled. (a) Steeply dipping fault plane showing well-expressed striae. (b) Stereoplot of the structural data, the direction of paleostress obtained by inversion is indicated by the white arrows. (c) Close-up photo of the fault plane showing (d) the sampling site.

characterized by a Moho shallowing of ~15 km with respect to the surrounding regions [e.g., *Benoit et al*., 2006; *Keranen and Klemperer*, 2008; *Keranen et al*., 2009] (Figure 1). Following this rifting event, the activity of a mantle plume(s) in Eocene-early Oligocene triggered the emplacement of a thick sequence of trap basalts [e.g., *Mohr and Zanettin*, 1988], which lie on top of either Mesocenozoic sediments in the north or the basement in southern Ethiopia (Figure 1).

3. Geology of Southern Ethiopia

The basement is the oldest unit outcropping in southern Ethiopia [*Davidson*, 1983; *Abraham*, 1989] and consists of highly deformed gneisses, amphibolites, and granulites interlayered with plutonic rocks of Archean to Proterozoic age [e.g., *Davidson*, 1983; Geological map of Ethiopia, *Mengesha et al*., 1996]. A penetrative foliation is associated to this deformation, which displays different relations with the rift structures (Figure 2). Tertiary sandstones unconformably overlie the basement and have been interpreted to result from erosion of basement rocks during Tertiary times [*Ebinger et al*., 1993].

Transitional tholeiitic basalt flows and subordinate tuffs compose the trap series in the area (Gamo-Amaro basalts of *Ebinger et al*. [2000]). This series widely outcrops above the basement in southern Ethiopia and have been dated between 48 and 30 Ma. The flood basalt sequences may reach current thicknesses exceeding 1000 m in this area.

No major phases of extension and rift basin subsidence affected the region north of Lake Turkana between ~45 and ~20 Ma [*Ebinger et al*., 2000]. An early phase of rifting occurred in the Miocene and gave rise to the development of border faults in the Chew Bahir–Gofa Province, as well as in the sMER [e.g., *Wolde-Gabriel et al*., 1991; *Ebinger et al*., 1993, 2000]. This extensional event triggered basaltic dyking at 20–21 Ma (Chencha escarpment [*Bonini et al*., 2005] and western margin of the Amaro horst [*Levitte et al*., 1974]), as well as a phase of basement exhumation with onset at 20 ± 2 Ma (Chew Bahir area, (U/Th)He on apatite [*Pik et al*., 2008]). At 18–14 Ma, the rifting was well established in the region as (i) interbedded basaltic flows and lacustrine sediments deposited within the rift floor (southern end of the Amaro horst, southwest of the Galana basin; Figure 2 [*Wolde-Gabriel et al*., 1991; *Ebinger et al*., 1993]) and (ii) an ~14 Ma volcanic center aligned along border faults [*Ebinger et al*., 1993, 2000]. At ~20–11 Ma, volcanic activity (Getra-Kele basalts of *Ebinger et al*. [1993, 2000]) accompanied this extensional phase, which has been associated with the northward propagation of the N-S striking Kenyan rift [*Bonini et al*., 2005].

An ~10 Ma, hiatus followed this first (Kenyan rift-related) rifting event [e.g., *Ebinger et al*., 2000; *Bonini et al*., 2005], and major volcanic activity was then resumed in the sMER with the eruption of Pliocene peralkaline pantelleritic ignimbrites that are time correlative with the Nazret pyroclastic rocks of the nMER and cMER [*Abebe et al*., 2005]. These volcanics are believed to mark the onset of rifting in the MER [*Bonini et al*., 2005]. The most recent rocks consist of late Pliocene to recent lacustrine sediments and volcanic products. These

Table 1. Structural Measurements and Results of Paleostress Analysis Obtained From Inversion of the Field Data[a]

Site	Number of Data	Latitude	Longitude	Age of the Youngest Deformed Rock	n/nt	σ_1	σ_2	σ_3	R'	α_w	QRw
1	8	7.280670	38.501920	*Quaternary*		58/123	11/12	275/28	0.97	8.29	D
2	6	6.96699	38.30636	*Quaternary*	1	269/50	1/2	94/39	1.16	3.1	D
3	1	6.94435	38.26381	*Quaternary*	1	105/74	13/0	283/16	0.5	-	E
4	*8*	*6.90453*	*38.39361*	*Upper Pleistocene*	*1*	*252/61*	*21/19*	*118/21*	*0.62*	*3.8*	*D*
5	11	6.7993	38.34515	*Quaternary*	0.73	93/60	194/6	287/29	0.76	11.8	D
6	14	6.96831	38.06022	*Quaternary*	0.57	358/34	216/49	102/20	1.5	6.8	D
7	*18*	*6.70758*	*38.21208*	*Upper Pleistocene*	*0.29*	*335/86*	*215/2*	*125/4*	*0.58*	*10.9*	*E*
8	3	6.70236	38.25211	*Quaternary*	1	267/53	358/1	88/39	0.5	-	E
9	4	6.69015	38.36153	*Quaternary*	1	329/68	158/21	67/3	0.58	28.5	E
10	6	6.37105	38.17802	*Eocene*	1	42/80	171/6	262/7	0.31	16.4	D
11	8	6.364617	38.321433	*Eocene*	1	109/73	201/1	291/17	0.67	5.0	D
12	16	6.38636	37.08751	*Quaternary*	1	259/76	27/9	119/11	0.36	10.1	B
13	22	6.29583	36.855	*Quaternary*	0.59	282/65	13/0	103/25	0.76	7.0	C
14	9	6.26165	37.01119	*Quaternary*	1	286/68	20/2	111/22	0.84	5.3	D
15	16	6.20473	37.71857	Quaternary	0.94	200/73	38/16	307/5	0.49	9.0	C
16	19	6.12775	37.62472	Quaternary	0.58	18/78	210/11	120/2	0.82	13.5	C
17	*7*	*6.12513*	*37.57452*	*Holocene*	*1*	*293/68*	*34/4*	*125/22*	*0.55*	*11.7*	*D*
18	15	6.11185	37.55945	*Quaternary*	1	262/58	353/1	84/24	0.75	11.1	B
19	16	6.0434	37.54395	*Quaternary*	0.63	286/57	20/3	112/35	1.04	9.0	C
20	*15*	*5.99259*	*37.53829*	*Upper Pleistocene*	*0.73*	*354/82*	*230/4*	*140/6*	*0.42*	*4.7*	*C*
21	6	5.9716	37.65049	*Eocene*	0.83	151/69	54/2	323/20	0.7	8.6	E
22	3	5.91193	37.71001	*Eocene*	3	304/36	158/48	48/17	1.22	-	E
23	5	6.13743	38.125	*Eocene*	0.8	269/57	178/1	87/33	0.93	4.4	E
24	4	6.14845	38.1242	*Eocene*	0.5	255/62	1/8	95/27	0.77	-	E
25	12	6.15158	38.1782	*Eocene*	1	295/75	193/6	101/18	0.54	9.1	C
26	9	5.900600	38.167300	*Eocene*	0.67	61/49	161/9	253/14	0.62	4.0	D
27	18	5.931700	38.230967	*Eocene*	0.44	274/55	6/1	97/35	1.16	5.1	D
28	14	6.143718	36.958265	*Quaternary*	0.83	221/53	356/28	98/22	0.76	19.1	C
29	5	6.077386	36.906652	*Quaternary*	1	14/70	236/15	143/13	0.5	18.0	E
30	23	6.058517	36.866667	*Quaternary*	1	292/67	40/8	133/22	0.57	10.3	B
31	22	5.982117	36.811733	*Quaternary*	0.5	317/74	61/4	152/16	0.51	5.6	C
32	5	5.904650	36.736917	*Quaternary*	1	319/66	223/2	132/24	0.87	-	E
33	8	5.833750	36.666850	*Quaternary*	1	308/62	43/2	134/28	0.79	7.8	D
34	11	5.826450	36.652833	*Quaternary*	1	268/70	22/9	115/18	0.66	11.6	C
35	9	5.773938	36.792467	*Quaternary*	1	294/65	38/7	131/25	0.57	6.9	D
36	2	5.620278	36.859722	*Quaternary*	1	318/67	218/4	126/22	0.64	-	E
37	7	5.441200	36.923100	*Quaternary*	1	164/63	59/8	325/26	0.29	4.2	D
38	10	5.433800	36.932700	*Quaternary*	0.7	315/65	198/12	104/22	0.41	2.1	D
39	8	5.618267	37.322267	*Quaternary*	0.88	187/39	279/3	nov-27	0.21	6.8	D
40	4	5.320050	36.927367	*Quaternary*	1	252/65	350/4	81/24	0.83	-	E
41	15	5.272267	36.909067	*Quaternary*	0.8	278/68	142/26	47/14	0.13	7.6	C
42	8	5.112917	36.850250	*Quaternary*	0.88	245/60	338/2	69/30	0.8	8.5	D
43	5	5.076712	36.846422	*Quaternary*	1	220/57	51/32	318/5	0.38	-	E
44	8	4.958275	36.730033	*Quaternary*	0.75	252/72	354/4	86/18	0.41	4.56	E
45	23	4.829750	36.724667	*Quaternary*	0.43	13/38	222/48	115/15	1.24	9.7	B

[a]Dated fault gouges are indicated in bold italic. The age of the youngest deformed rock is taken either from the geological map of Ethiopia [*Mengesha et al.*, 1996] in italic or from the Omo River project map [*Davidson*, 1983] in plain text. The n/nt is the ratio between total number of data and the number of data fitting the calculated tensor, $\sigma_1 \geq \sigma_2 \geq \sigma_3$ are the principal stresses, α_w is the average slip deviation between the measured and calculated slips, R' is the stress regime index, and QRw is the world stress map quality rank ranging from A: very good to E: very poor.

deposits are strictly related to fault activity that characterizes portions of the rift (e.g., Nech Sar, Segen, and Mursi basalts) [e.g., *Ebinger et al.*, 2000].

Existing data on fault kinematics consist of both (i) field measurements of slickensides on fault planes and their inversion for paleostress reconstructions and (ii) analysis of available focal mechanisms. Focal mechanisms give *T* axes trending around 90°N in the Abaya region and around 130°N in the Chew Bahir (Figure 2; Harvard centroid moment tensor (CMT) catalog [*Foster and Jackson*, 1998; *Ayele and Arvidsson*, 1998]). The analysis of fault kinematics and paleostress reconstruction shows a stretching direction varying from N90°E to N120°E [*Boccaletti et al.*, 1998; *Bonini et al.*, 2005; *Agostini et al.*, 2011](Figure 2).

Table 2. Results of Paleostress Analysis Obtained From Inversion of the Field Data Per Regions and Along Single Faults[a]

	Region	Number of Data	n/nt	σ_1	σ_2	σ_3	R'	α_w	QRw	QRt
Figure 4	North Abaya	283	0.60	279/74	16/2	107/16	0.33	11.36	A	A
	Lakes Abaya-Chamo	182	0.94	251/86	4/2	94/4	0.03	11.09	B	C
	Gofa Province	145	0.74	277/71	30/8	123/18	0.32	12.37	C	D
	Chew Bahir	71	0.65	4 1/2	19/7	113/28	0.4	5.76	A	E
Figure 5	7 to 9	25	0.48	346/62	192/26	97/11	0.24	5.63	D	D
	10 and 11	14	0.71	86/65	181/03	273/25	0.36	4.15	C	E
Figure 6	12 and 14	25	0.76	229/72	0/12	93/14	0.26	8.26	B	D
	27 and 26	27	0.53	277/54	186/0	96/36	0.66	4.79	D	E
Figure 7	28 to 32	69	0.73	314/71	51/3	142/18	0.35	9.63	B	D
Figure 8	44 and 45	31	0.58	292/52	27/4	120/37	0.72	9.72	B	E

[a]The n/nt is the ratio between the total number of data and the number of data fitting the calculated tensor, $\sigma_1 \geq \sigma_2 \geq \sigma_3$ are the principal stresses, α_w is the average slip deviation between the measured and calculated slips, R' is the stress regime index, QRw is the world stress map quality rank, and QRt is the tensor quality rank ranging from A: very good to E: very poor.

4. Structure and ^{14}C Dating of the Different Rift Sectors

In order to characterize the geometry, kinematics, and timing of faulting, the area has been investigated during extensive fieldwork campaigns from 2007 to 2013. Fault slip data consist of measurements of fault planes and slickenlines (Figures 3a and 3b), and data sets contain up to 23 measurements at some sites, with an average of 10 measurements per site (Table 1). The uncertainties of the measurement during data acquisition in the field are approximately 5°. Fault slip data have been collected to compute paleostress tensors using WinTensor [*Delvaux and Sperner*, 2003], based on the dihedron inversion method [*Angelier and Mechler*, 1977; *Angelier*, 1979] and rotational optimization of the obtained tensor. The quality of the stress inversion is given by quality rank, which ranges from A (very good) to E (very poor). The QRw (World Stress Map quality rank) depends on the average slip deviation angle (α_w) and the percentage of used measurement to compute the tensor out of the total amount of data (n/nt), whereas the spatial dispersion of the data is also taken into account when estimating the QRt (tensor quality rank)[*Delvaux and Sperner*, 2003]. Our data set is rather homogeneous in terms of both strike and slip; therefore, we provided only the QRw for individual sites (Table 1). When merging the individual sites either to perform regional inversions per area (Figure 4) or to perform inversions of clusters of data along the same fault (Figures 5–8), the spatial dispersion of the data is higher. Consequently, the calculated tensor has a good quality and ranges between A and D (Table 2).

Orientation data (e.g., foliation of basement rocks, fault slip, and plane) are displayed as stereoplots using OSXStereonet [*Allmendinger et al.*, 2011; *Cardozo and Allmendinger*, 2013] (Table 1). Furthermore, fault gouges and basement rocks have been sampled for radiocarbon dating (Tables 1 and 3) and apatite fission tracks analysis (see section 5), respectively.

Organic matter within the faulted debris has been sampled for radiocarbon dating to provide indications of the maximum age for the latest movement on the fault plane (Figures 3c and 3d). The preparation of samples for AMS (accelerator mass spectrometry) radiocarbon dating consisted of a pretreatment during which any contaminants, which could bias the radiocarbon dating result, were removed. This was followed by the carbon extraction and conversion into a solid graphite target suitable to be used as a cathode in the sputtering ion source of the AMS. For the samples that provided at least 1 mg of graphite after the removal of

Table 3. ^{14}C Radiometric Ages of Faulted Debris[a]

Site	Locality	Latitude	Longitude	Lithology	Radiocarbon	Calibrated Age (2δ)
4	Irba	6.90453	38.393611	Debris^	30842 ± 700	
7	Gado	6.70758	38.212083	Debris^	14280 ± 100	15810 B.C. (95.4%) 15040 B.C.
17	Chencha fault	6.12513	37.574517	Debris^	6896 ± 50	5900 B.C. (95.4%) 5660 B.C.
20	Arba Minch	5.99259	37.538292	Debris^	26174 ± 100	
20	Arba Minch	5.99259	37.538292	Debris^	23922 ± 150	

[a]Analysis done by the CEDAD, Dipartimento di Ingegneria dell'Innovazione, Università del Salento, Lecce, Italy, http://www.cedad.unisalento.it/en/.

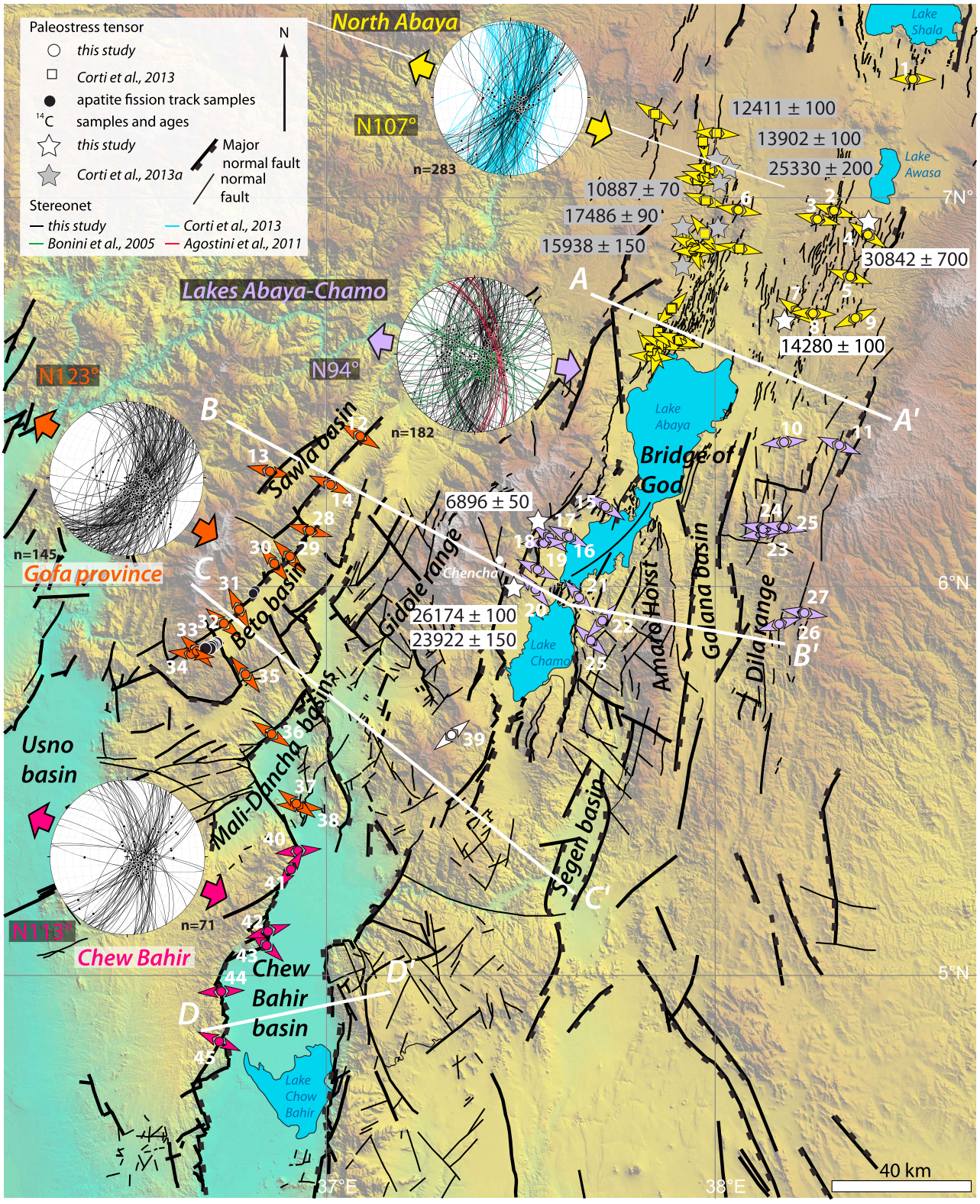

Figure 4. Rift-related fault pattern in southern Ethiopia superposed on a SRTM digital elevation model. Results of paleostress analysis in each measurement site are illustrated as colored arrows; the different colors refer to the different regions (and subregions) described in the text as follows: yellow: sMER-North Abaya, purple: sMER-Lakes Abaya-Chamo, orange: Gofa Province, and pink: Chew Bahir. Stereoplot display of the fault planes and the associated fault slip vectors grouped by area (black line: data from this study, blue lines: from *Corti et al.* [2013b], red lines from *Agostini et al.* [2011], and green lines from *Bonini et al.* [2005]; colored arrows indicate the obtained direction of extension. The ^{14}C ages are indicated by white (this study) or gray [from *Corti et al.*, 2013b] stars.

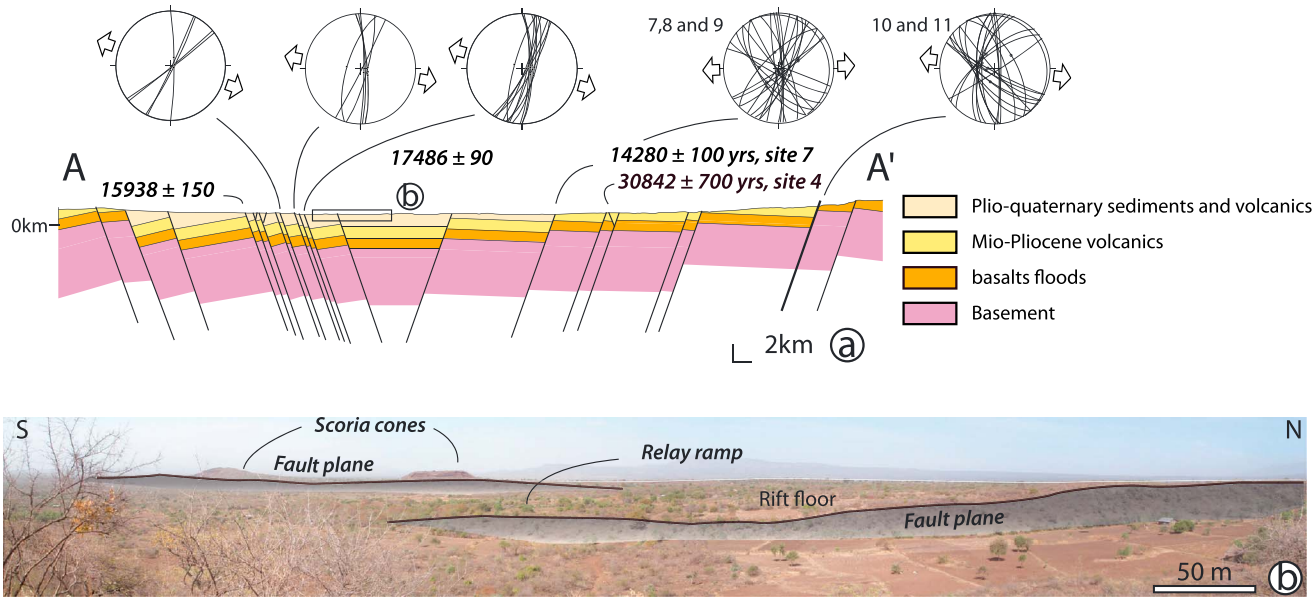

Figure 5. (a) Cross section AA′ cutting trough the north Abaya area. Stereoplot display of the fault planes and the associated fault slip vectors. White arrows indicate the obtained direction of extension. ^{14}C dating of debris-rich fault gouge are indicated in bold. (b) Panorama of the rift floor showing a relay-ramp between small normal faults associated with volcanic edifices that are characteristic of the north Abaya area.

contaminants, high-resolution mass spectrometry ^{14}C dating was performed by CEDAD (Table 2) (Centro di Datazione e Diagnostica, Dipartimento di Ingegneria dell'Innovazione, Università del Salento, Lecce, Italy, http://www.cedad.unisalento.it/en/). The standard precision in the measurement of $^{14}C/^{12}C$ ratio was 0.5% for samples aged less than 2000 years old, which means a standard deviation of ±40 years.

Following previous works [e.g., *Ebinger et al.*, 2000], the rift in southern Ethiopia has been subdivided in three main sectors: (i) the sMER, (ii) the Gofa Province, and (iii) the Chew Bahir (Figure 4). The sMER has been further subdivided into two subregions: the north Abaya region and the Lakes Abaya-Chamo area. These rift sectors display a distinctive fault pattern; from north to south, fault length is increasing (15 km in the sMER to 50 km in the Gofa Province and the Chow Bahir area) as well as fault spacing (1 km in the sMER to 10 km in the Gofa Province and the Chow Bahir area). Moreover, paleostress inversion of fault sip data in the different sectors gives similar orientation of the stretching direction apart from Gofa Province (Figure 4), as illustrated and discussed in the following sections. The overall geometry, kinematics, and timing of the deformation of the BRZ is illustrated by four cross sections orthogonal to the trend of the main faults, together with the kinematics and, when constrained, ^{14}C ages of the smeared debris (see location in Figures 2 and 4 and Tables 1 and 3 for fault kinematics and dating). The sections are discussed from north to south (Figures 4–7).

4.1. sMER: North Abaya Area

In the north Abaya region, the volcanotectonic activity is mostly accommodated at the western margin of the ~90 km wide rift. This margin is affected by numerous, closely spaced, small normal faults that strike ~N20°–25°E and widespread Pleistocene-Holocene volcanism [*Corti et al.*, 2013a]. The rift floor is affected by few internal faults striking ~N10°E. In the western margin, radiocarbon dating yields ages between 10 and 25 kyr on the border faults [*Corti et al.*, 2013a]. New radiocarbon analysis of smeared debris collected along faults on the eastern margin gives ages of 14 kyr (Site 7, Figure 4; Tables 1 and 3) and 31 kyr (Site 4, Figure 3; Tables 1 and 3), thus supporting a late Quaternary activity of the fault system. The elaboration of the whole fault data set—consisting of new fault slip data collected on the eastern margin and existing data on the western margin (see yellow arrows in Figure 4)—indicates an overall ~N105°E directed extension.

Cross section AA′, located north of Lake Abaya, highlights a different deformation style at the rift margins (Figure 5a). In particular, the western margin is characterized by a series of small length (~3 km)/limited offset (~100 m) east dipping normal faults, which accommodate a gradual transition between the rift floor and the plateau. These faults are typically en-echelon arranged in plain view, with faults connected to each other by

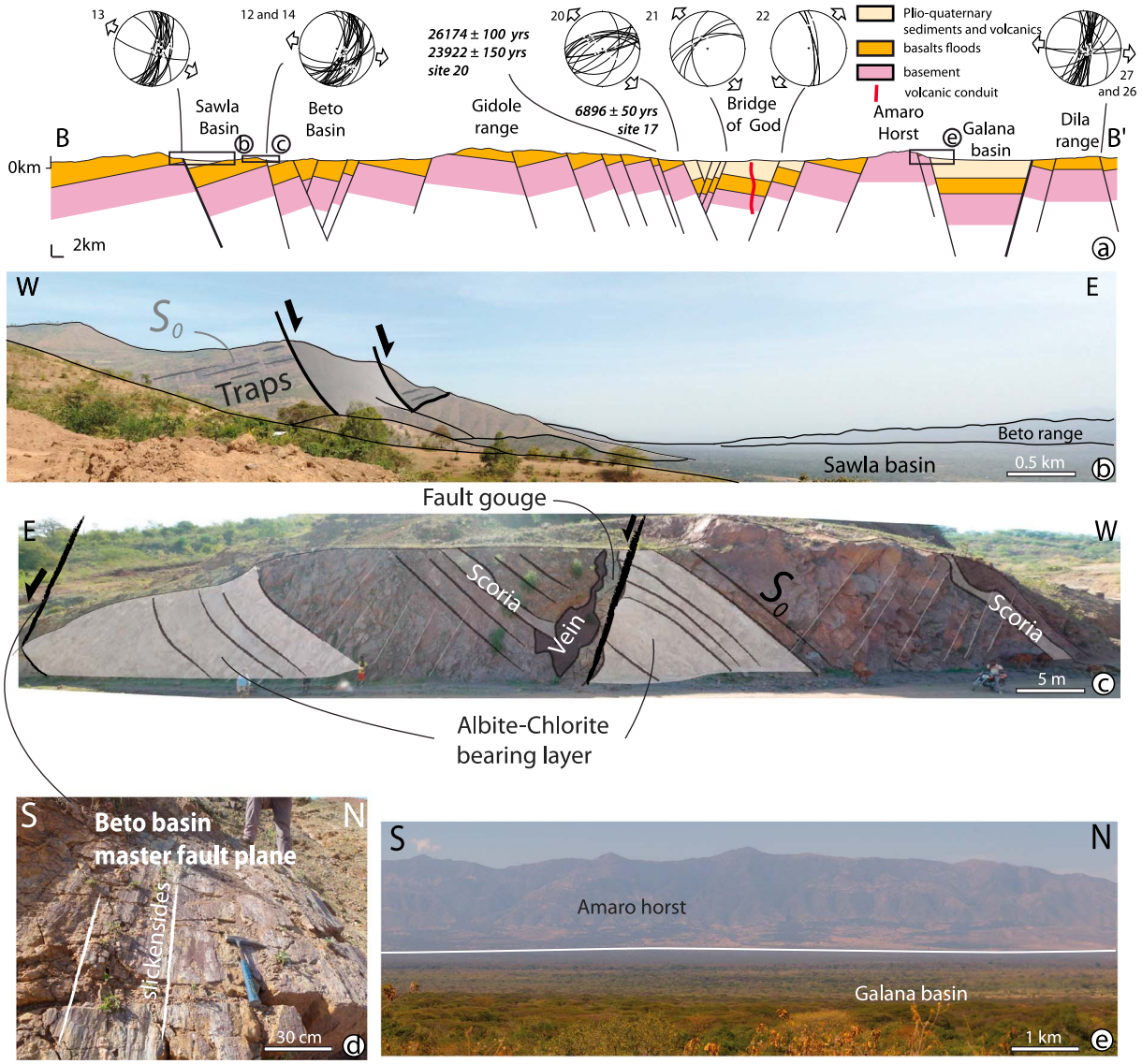

Figure 6. (a) Cross section BB' cutting trough the Lakes Abaya-Chamo region, illustrated in Figure 4. (b) Panorama of the Sawla basin showing major faults on the western margin, causing tilting of trap series (S_0), also shown in the Beto range to the east. (c) Deformation at the western margin of the Beto basin. The master fault is located at the eastern margin of the photograph, which clearly shows some secondary fault planes. Note that these secondary faults offset a scoria horizon and an albite-chlorite bearing layer by a few tens of meters. (d) Beto master fault plane showing dip-slip slickensides. (e) Panorama of the Amaro horst and the Galana basin.

relay ramps (Figure 5b). Significant volcanism is associated with this faulting, with numerous basaltic scoria cones and subordinate obsidian centers aligned along the faults [*Corti et al.*, 2013a]. Paleostress analysis on the faults points to a N107°E direction of extension (Table 2 and yellow arrows in Figure 4). The eastern margin is instead characterized by a sharper transition with less numerous west dipping faults, whose footwall exposes the trap series.

4.2. sMER: Lakes Abaya and Chamo

In the Lakes Abaya and Chamo area, the rift bifurcates into two basins separated by the N-S trending Amaro Horst (Figure 2). The rift in this region is delimitated by few, widely spaced, and large normal faults that strike ~N0°–25°E. Internal faults are almost absent, apart from the normal faults that affect the recent volcanic products (Nech Sar basalts) of the Bridge of God, which separates Lakes Abaya and Chamo. New radiocarbon dating of the fault gouge collected along the western margin indicates ages of ~26 kyr to 23 kyr (Site 20, Figure 4; Tables 1 and 3) and 7 kyr (Site 17, Figure 4; Tables 1 and 3), thus supporting late Pleistocene-Holocene

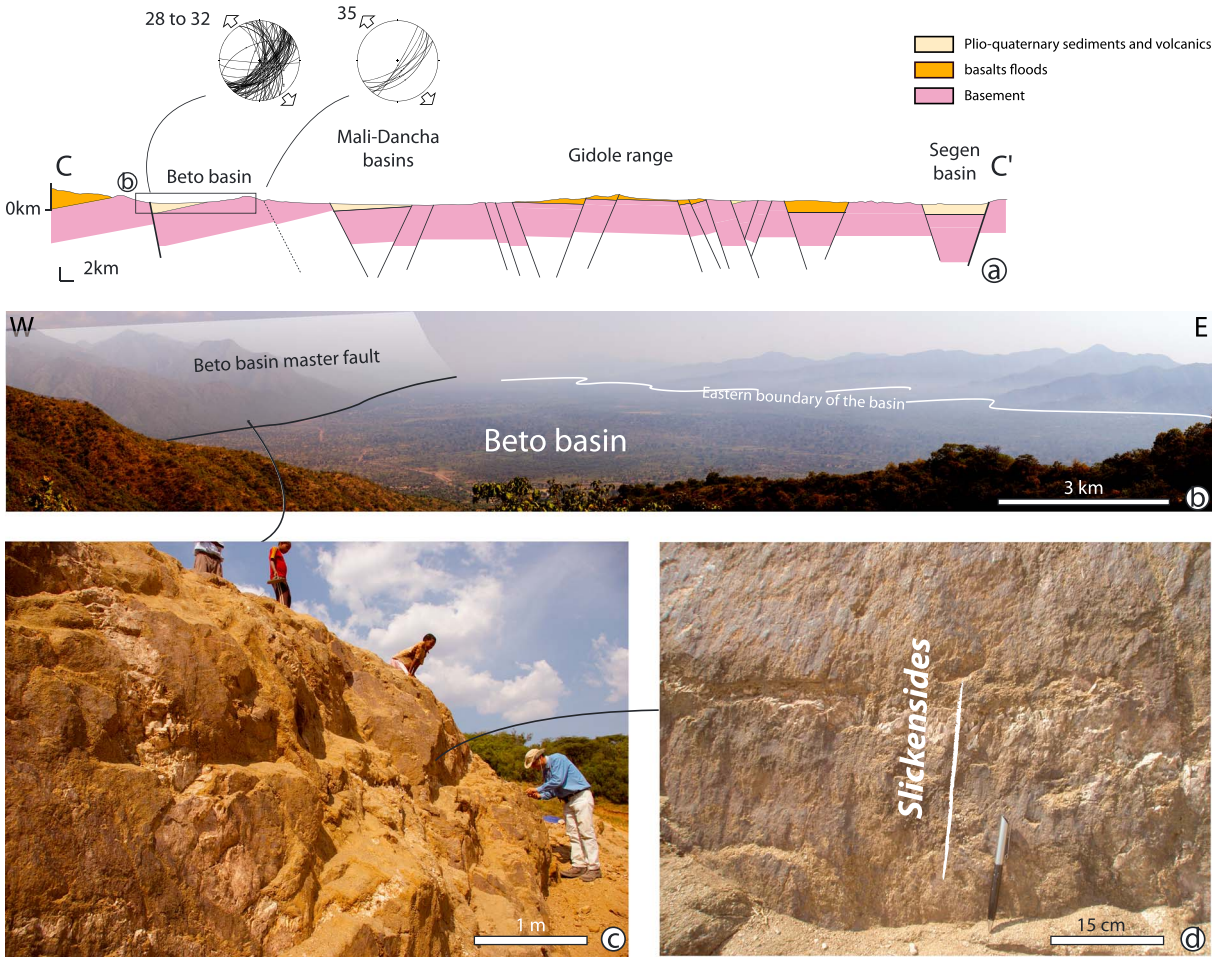

Figure 7. (a) Cross section CC′ cutting through the Gofa area, Gidole range, and Segen basin, illustrated as in Figure 4. (b) View of the Beto basin showing the master fault on the western margin. (c) Close-up photo of the Beto master fault plane that crops out close to the Beto village. Sample GR2 used for low-temperature thermochronology has been collected at this location (Table 4). (d) Close-up picture of the fault plane showing dip-slip slickensides.

activities. Paleostress inversion of the whole fault data set in this region yields an overall ~N94°E directed extension (Table 2 and purple arrows in Figure 4).

Cross section BB′ (Figure 6a) extends from the Sawla basin in the west (pertaining to the Gofa Province described in more detail in the following section) to the Dila range in the east, cutting through the Bridge of God. In this area, the rift widens to reach a width of ~170 km in correlation with a thinning of the crustal thickness occurring south of the Goba Bonga line (see below section 4.5; Figure 1). The cross section displays four different basins: two in the sMER (Abaya-Chamo and Galana) and two in the Gofa Province (Sawla and Beto). Notably, the two sMER basins are characterized by a roughly symmetric structure, whereas the two basins in the Gofa Province are asymmetric (Figure 6a). In the Sawla basin, the border fault is steep, and the trap series is dipping ~20° toward the west (Figure 6b). The master fault bounding the Beto basin tilts the trap series of about 20° (Figure 6a) and locally up to ~40° to the west (Figure 6c). The fault plane shows well-expressed dip-slip kinematic indicators (Figure 6d). The east dipping border fault of the Abaya-Chamo basin is associated with paleostress direction trending N150°E. Two symmetric horsts made of basement and traps are outcropping along the cross section, specifically (1) the Gidole range, between Beto and Abaya-Chamo basins, and (2) the Amaro horst, located between the Abaya-Chamo and the Galana basins. The master fault bounding the Amaro horst to the east is poorly exposed, and no clear fault planes have been found (Figure 6e).

4.3. Gofa Province

The Gofa Province includes a series of subparallel basins west of the sMER [*Moore and Davidson*, 1978]. Most of these basins are half grabens [*Ebinger et al.*, 2000], showing a roughly triangular shape in plain view, with

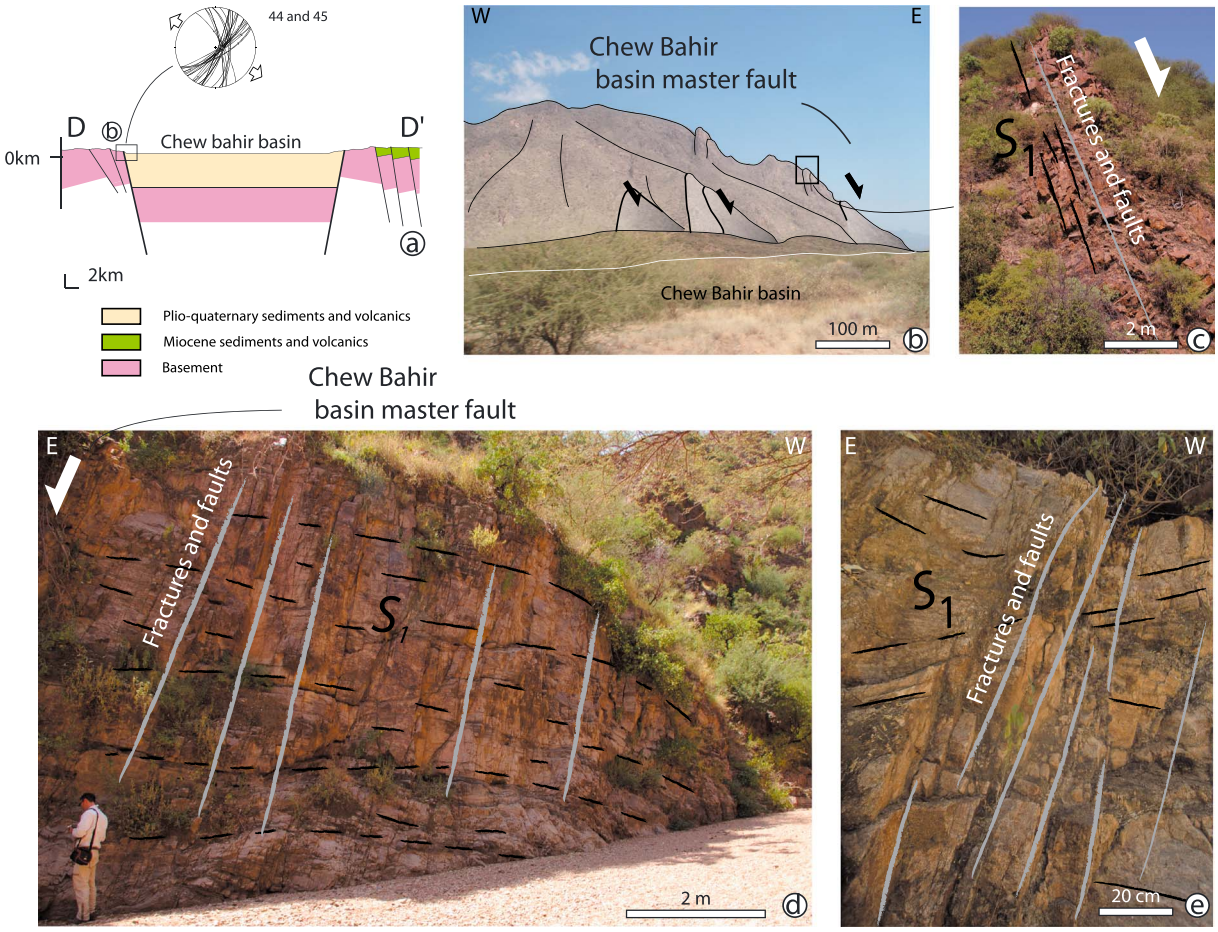

Figure 8. (a) Cross section CC′ cutting trough the Chew Bahir basin, illustrated as in Figure 4. (b) Photograph of the western margin of the Chew Bahir basin showing the main master fault. (c) Relation where the foliation is parallel to the fault plane. (d) Close-up photo of an outcrop where the foliation is flat lying and crosscut at high angle by the faults. (e) Close-up photograph showing the flat lying gneissic foliation S_1 cut by fractures and small faults.

widening of the basins toward the south. The 5 km wide ranges of basement rocks, which are covered by the trap series, separate the basins. Their western margin consists of large ~N40°E striking and east dipping normal faults; some of these faults are highly segmented with ~N150°E striking fault segments that locally delimit the basins to the south (Figures 2 and 4). Although no radiocarbon dating of fault gouge is available for this area, geomorphologic analysis points to a very recent activity of the main faults in the Gofa province (see section 6 below). Paleostress inversion of the whole fault data set in the Gofa Province shows a mean ~N123° trending extension direction (Table 2 and orange arrows in Figure 4).

Cross section CC′ extends from the Beto to the Segen basin cutting through the Gidole range (Figure 7a). Well-exposed east dipping master faults bound the asymmetric Beto and Mali-Dancha basins; to the east, the deposits filling the Beto basin unconformably onlap directly the basement (Figure 7b). Paleostress analysis indicates an ~N105°E and ~N135°E—trending extension directions for the master faults of both the Beto and Mali-Dancha basins, respectively (Figures 7c and 7d). In the central part of the section, the Gidole horst separates the Gofa Province basins from the sMER, which is represented by the roughly symmetric Segen basin, filled by syn-rift deposits.

4.4. Chew Bahir

The Chew Bahir basin is delimited by large normal faults with an overall N-S strike. Unlike the Gofa Province basins, the Chew Bahir basin is roughly symmetric (cross section DD′; Figure 8a) and characterized by a minor increase in width to the south. The main faults are highly segmented and characterized by large-fault segments striking between NW-SE and N-S, alternated with smaller ENE-oriented faults. Although this pattern

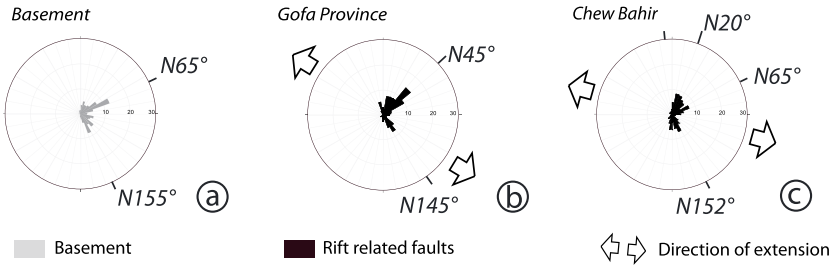

Figure 9. Control of preexisting weak zones on the rift-related deformation pattern. Stereoplot with rose diagrams of (a) the trend of basement structures and (b and c) faults in the Gofa Province and the Chew Bahir area, respectively.

reflects a control by preexisting heterogeneities at a regional scale (Figure 8a) [e.g., *Corti*, 2009], at local scale, the relationship between the main foliation affecting the basement rocks (S_1) and the faults and fractures is less straightforward (Figure 8). When S_1 is favorably oriented, this fabric may be reactivated by faults (Figures 8b and 8c), whereas when S_1 is gently dipping or unfavorably oriented, it is not reactivated but it is crosscut by high-angle normal faults (Figures 8d and 8e). The border faults are characterized by prominent morphological expressions, and the distribution of local seismicity points to ongoing activity of these structures [e.g., *Boccaletti et al*., 1998; *Ayele and Arvidsson*, 1998; *Ebinger et al*., 2000]. The (U-Th)/He thermochronometry suggests a Miocene age of basement exhumation in the area [*Pik et al*., 2008]. Paleostress inversions determined on differently oriented fault segments give extension directions trending roughly orthogonal to the fault strike (Figure 4, Sites 40 to 45). However, paleostress inversion of the whole fault data set shows an overall ~N113°E directed extension that is roughly orthogonal to the axis of the Chew Bahir basin (Table 2 and pink arrows in Figure 4).

4.5. Relations Between Fault Development and Preexisting Discrete Heterogeneities

Detailed analysis of the structures based on both remote and field data shows that fractures and the penetrative foliation in the basement have two main trends, which are orthogonal to each other: ~N65°E and ~N155°E, respectively (Figure 9a). These two families of structures are considered to be preexisting as their orientation is close to that of the MOSZ and the trend of the Mesozoic basins, respectively (Figure 1). The rift-related fault pattern in the Gofa Province shows two fault systems that trend ~N45°E and ~N145°E (Figure 9b); similarly, two orthogonal major fault sets, trending ~N65°E and ~N150°E, characterize the Chew Bahir basin (Figure 9c). This shows that preexisting basement structures strongly controlled the rift-related fault pattern in the Gofa Province and the Chew Bahir basin. East of the Gofa Province and Chew Bahir areas and elsewhere in the sMER, the faults are trending roughly NNE and show little correlation with the basement structures. This noncorrelation can be explained by a change in the trend of the basement structures from west to east, coherent with the transition from the Neoproterozoic mobile belts to the west to the Archean terranes to the east [*Kazmin et al*., 1978; *Stern*, 1994, 2002].

5. Apatite Fission Track Analysis: Basement Exhumation in the Gofa Province

Fault gouges in the Gofa Province do not contain organic matter, consequently ^{14}C dating is not feasible in the area. However, the rift-related exhumation of the basement can be constrained with low-temperature thermochronology providing insight in the onset of rifting in the area. We use apatite fission track (AFT) thermochronology to constrain these late stages of basement exhumation along the southern ends of the Beto basin. Over geological time, fission tracks are fully retained in apatite at temperature below 60°C/10^4 m, while they are only partially retained between 60°C/10^4 m and 120°C/10^4 m (partial annealing zone (PAZ)) with a mean closure temperature of 110°(±10)°C/10^4 m [*Green and Duddy*, 1989].

Granitoids and gneiss belonging to the Pan-African basement surrounding the Beto basin have been sampled in two locations (Figure 10): (1) a vertical profile composed of eight samples (GR4-11) from the footwall of the fault delimiting the Beto basin to the south (the vertical distance of the profile is ~700 m, from an altitude of 1238 m to 1949 m) and (2) two further samples (GR2 and GR3, with elevation of 1115 m and 1214 m, respectively) collected in the lowest (exposed) part of the footwall of the east dipping master fault bounding the Beto basin. AFT dating along the vertical profile yielded central ages between 75.5 ± 4.7 Ma and

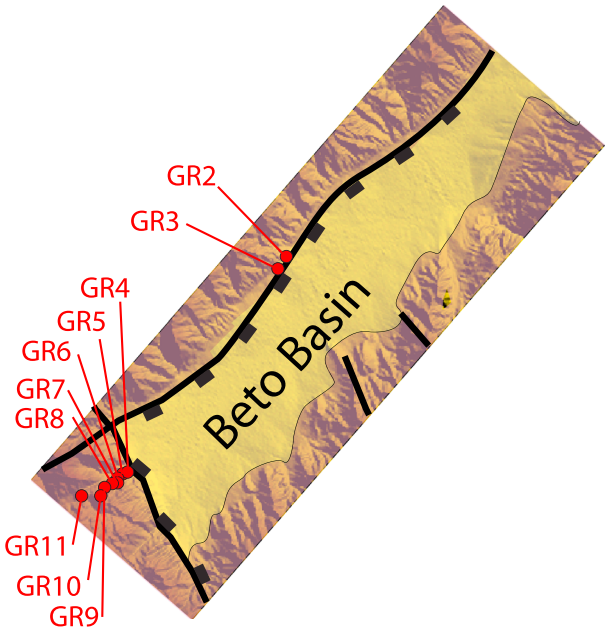

Figure 10. Map of the Beto basin showing the location of fission track samples.

59.2 ± 7.9 Ma (Table 4). This age range is consistent with a significant continent-wide exhumation event at 60–75 Ma recorded in Kenya, that might reflect the Mesocenozoic rifting that affected the whole eastern Africa [*Foster and Gleadow*, 1996; *Spiegel et al*., 2007]. The two northern samples (GR2 and GR3) show young AFT ages of 7.0 ± 0.7 Ma and 11.3 ± 0.8 Ma.

Thermal modeling of the AFT ages [*Gallagher*, 1995; *Ketcham et al*., 2000; *Ketcham*, 2005] was performed with HeFTy program [*Ketcham et al*., 2007b]. For each modeled sample, the obtained time-temperature histories are shown (Figure 11, left). The program defines envelopes in a time-temperature space containing all paths that statistically yield "good" and "acceptable" fits with observed data. The dark gray regions envelope all the statistically good fit paths, while the light gray regions envelope the acceptable fit paths. The thick black line represents the best fitting path. Modeled and measured ages and track lengths for the best fitting path for each sample are reported (Figure 11, right). Usually, modeling is performed on sample with a consistent number of measured track length (i.e., ≥50). Only TINTs (tracks reached by the etching because they intercept a surface track [*Bhandari et al*., 1971]) made part of the measured length distributions as recommended by *Ketcham* [2005]. For this reason, we excluded sample GR5. Instead, we are showing the modeling of sample GR3, where only 25 TINTs were measured, but a total of 58 TINTs + TINCLEs (tracks reached by the etching through a cleavage) were measured. Thermal modeling of the southern samples shows that a prerift cooling event likely occurred at about 70–75 Ma in this area coherent with previous findings [*Foster and Gleadow*, 1996; *Spiegel et al*., 2007](Figure 11). The presence of these "old" ages recording a prerift history means that the rocks now exposed on the footwall of the southern Beto basin master fault were not buried deep enough by the flood basalts to be at temperatures below the bottom of the PAZ. The presence of Eocene flood basalts close to the profile and with an estimated thickness of Paleocene plus Miocene volcanic strata exceeding 1 km [*Ebinger et al*., 1993, 2000] requires that our samples have undergone a certain amount of heating. This heating event that started during the Paleocene has been taken into account in our models. Thermal modeling of our samples shows that they were heated at PAZ temperatures possibly reaching even 80°C around 40 Ma (that is especially well illustrated by samples GR11, GR9, and GR6), consistent with the current overburden of 1–1.5 km of Paleocene flood basalts, (Figure 11). Concerning the rift-related exhumation, the modeling of the "old samples" seems to indicate a late cooling in the late Neogene (Figure 11, GR11–GR6). This is in agreement with the two northern samples (GR2 and GR3) showing "young" AFT ages. The latter is accompanied by long-mean track lengths ($>$14 μm), which indicate an accelerated phase of cooling through the PAZ at that age (from late Miocene to present) as also confirmed by the modeling of GR3 (Figure 11). This late cooling is likely due to the denudation of the samples along the fault scarp and reflects the timing of the rift-related exhumation that led to Beto basin formation. The difference in sample age between the southern vertical profile and the base of the western scarp of the Beto basin can either be explained by (1) a different thickness of the volcanic cover above the basement, thicker for the samples at the base of the western scarp to bury the GR2 and GR3 samples below the base of the PAZ, or (2) by a different amount of rift-related denudation, higher for the base of the western scarp.

6. Geomorphology, Neotectonics, and Vertical Uplift

Interactions between (neo)tectonics and landscapes/landforms have been investigated by studying the geomorphology of the Gofa Province and the Chew Bahir area (Sawla, Beto, Mali, and northern Chew Bahir

Table 4. Apatite Fission Track Ages of the Basement Sampled in the Gofa Province[a]

Sample	Latitude	Longitude	El (m)	ρ_d	n_d	ρ_s	n_s	ρ_i	n_i	$P(\chi^2)$	Central Age (Ma)	U (µg/g)	Lm ± 1σ (µm)	SD (µm)	n_{TINTs} n	Lc ± 1σ (µm)	Dpar (µm)	SD
GR2	6.058567	36.88225	1115	7.16	5612	0.51	111	9.58	2069	89.7	7.0 ± 0.7	16	15.2 ± 0.8 14.5 ± 0.3*	1.13 0.94*	2 10*	-	2.4(76)	0.2
GR3	5.98045	36.81173	1214	7.16	5612	2.14	403	24.7	4647	21.4	11.3 ± 0.8	39	13.8 ± 0.3 14.2 ± 0.2*	1.33* 1.32*	25 58*	14.5 ± 1.2 14.8 ± 1.1*	2.5(100)	0.24
GR4	5.854933	36.71787	1238	7.16	5612	2.5	462	4.74	878	83.7	68.4 ± 5.0	8	12.3 ± 0.2	1.83	103	13.5 ± 1.3	3.4(93)	0.3
GR5	5.852533	36.71657	1290	7.16	5612	1.2	243	2.2	444	80.6	71.3 ± 6.3	3.6	12.1 ± 0.2	0.95	25	-	2.9(105)	0.3
GR6	5.852683	36.71348	1345	7.16	5612	10.4	1265	21.6	2623	0	60.2 ± 4.8	38	12.3 ± 0.2	1.9	101	13.5 ± 1.5	2.3(84)	0.2
GR7	5.848317	36.71163	1410	7.16	5612	3.66	503	7.58	1043	81.1	62.8 ± 4.1	14	12.3 ± 0.2	1.63	102	13.5 ± 1.5	3.1(80)	0.2
GR8	5.84775	36.70918	1528	7.16	5612	0.68	89	1.5	196	94.9	59.2 ± 7.9	2.7	-	-	-	-	2.5(73)	0.5
GR9	5.845267	36.70375	1632	7.16	5612	4.37	369	7.07	597	4.1	65.6 ± 5.4	15	13.3 ± 0.2	1.52	100	14.2 ± 1	2.5(78)	0.2
GR10	5.8402	36.7011	1745	7.16	5612	2.5	323	4.84	625	99.3	67.3 ± 5.2	11	13.4 ± 0.2	1.52	100	14.3 ± 1.2	2.6(98)	0.4
GR11	5.84	36.69022	1949	7.16	5612	9.38	958	16.1	1643	11.9	75.5 ± 4.7	28	12.8 ± 0.1	1.34	100	13.8 ± 1	2.4(81)	0.3

[a]Ages determined by external detector method using a zeta value for dosimeter CN5 $\zeta = 360 \pm 11$ (referred to Fish Canyon Tuff and Durango apatite standards, [*Hurford*, 1990]). El (m): sample elevations in meters; ρ_d, ρ_i: standard and induced track densities measured on mica external detectors; ρ_s: spontaneous track densities on internal mineral surfaces, track densities are given in 10^5 tracks cm^{-2}; n_d, n_i, and n_s: number of tracks on external detectors and on mineral surfaces; n_g: number of counted mineral grains; $P(\chi^2)$: (χ^2) probability [*Galbraith*, 1981]; central age calculated using TRACKKEY program [*Dunkl*, 2002]; Lm: mean length of confined tracks length distribution ± standard error, SD: standard deviation, and n_{TINTs}: number of TINTs (see text). Lm marked with the asterisk is distribution also composed by TINCLEs (see text) for the GR2 and GR3 samples, where due to the low track density, a few TINTs were available. Lc: mean length of the distribution of measured confined track lengths normalized for track angle using c axis projection [*Ketcham et al.*, 2007a, 2009]. Dpar: mean etch pit diameter parallel to the c axis for age grains. Dpar: mean etch pit diameter parallel to the c axis and number of total measured Dpar for sample. Samples were irradiated in the Lazy Susan facility of the Triga Mark II reactor of the University of Pavia (Italy).

basins; Figure 12a) focusing on hydrography (river longitudinal profiles) and general landforms of both footwall scarps and hanging wall basin floors. The aim of this analysis was to get information on the activity of extensional faults in areas where radiocarbon dating is not available.

In a wide range of climatic and geological settings, the topography of fluvial channels reveals that channel slope can be expressed as a power law function of contributing drainage area [*Hack*, 1957; *Flint*, 1974]:

$$S = k_s A^{-\theta} \quad (1)$$

where S is the local channel gradient, A is the contributing drainage area, k_s is the steepness index that measures channel gradient, and θ is the concavity index that describes the rate of change of channel gradient with drainage area [*Hack*, 1957; *Flint*, 1974; *Howard et al.*, 1994; *Willgoose et al.*, 1991; *Whipple and Tucker*, 1999]. Since θ and k_s are strongly dependent on many factors such as lithology, tectonic rates, and climate, their significance is still debated, although the dependence of the steepness index on rock uplift rate has been demonstrated [e.g., *Snyder et al.*, 2000; *Kirby and Whipple*, 2001; *Wobus et al.*, 2006; *Kirby et al.*, 2007]. On the contrary, theoretical considerations predict that the concavity index is independent of rock uplift rate, although many data point to a downstream change in channel concavity parallel to a variation in rock uplift rate [*Snyder et al.*, 2000; *Kirby and Whipple*, 2001; *Wobus et al.*, 2006]. Under steady state conditions, the θ value is expected to range between 0.4 and 0.6, normally ~0.45 [*Tarboton et al.*, 1989; *Snyder et al.*, 2000; *Kirby and Whipple*, 2001; *Whipple*, 2001, 2004; *Wobus et al.*, 2006; *Whipple et al.*, 2007]. Negative or >1 values indicate strong differences in uplift rates in time or space and are associated with knickpoints or knickzones [*Whipple*, 2004; *Schoenbohm et al.*, 2004; *Hoke et al.*, 2007]. These deviations from the concave-up shape indicate that the river is in a transient state of disequilibrium as a result of uplift rate variations triggered by tectonic and climatic factors or eustatic perturbations.

Fifty river profiles were extracted from the digital elevation model (DEM), and the relative indices have been calculated using

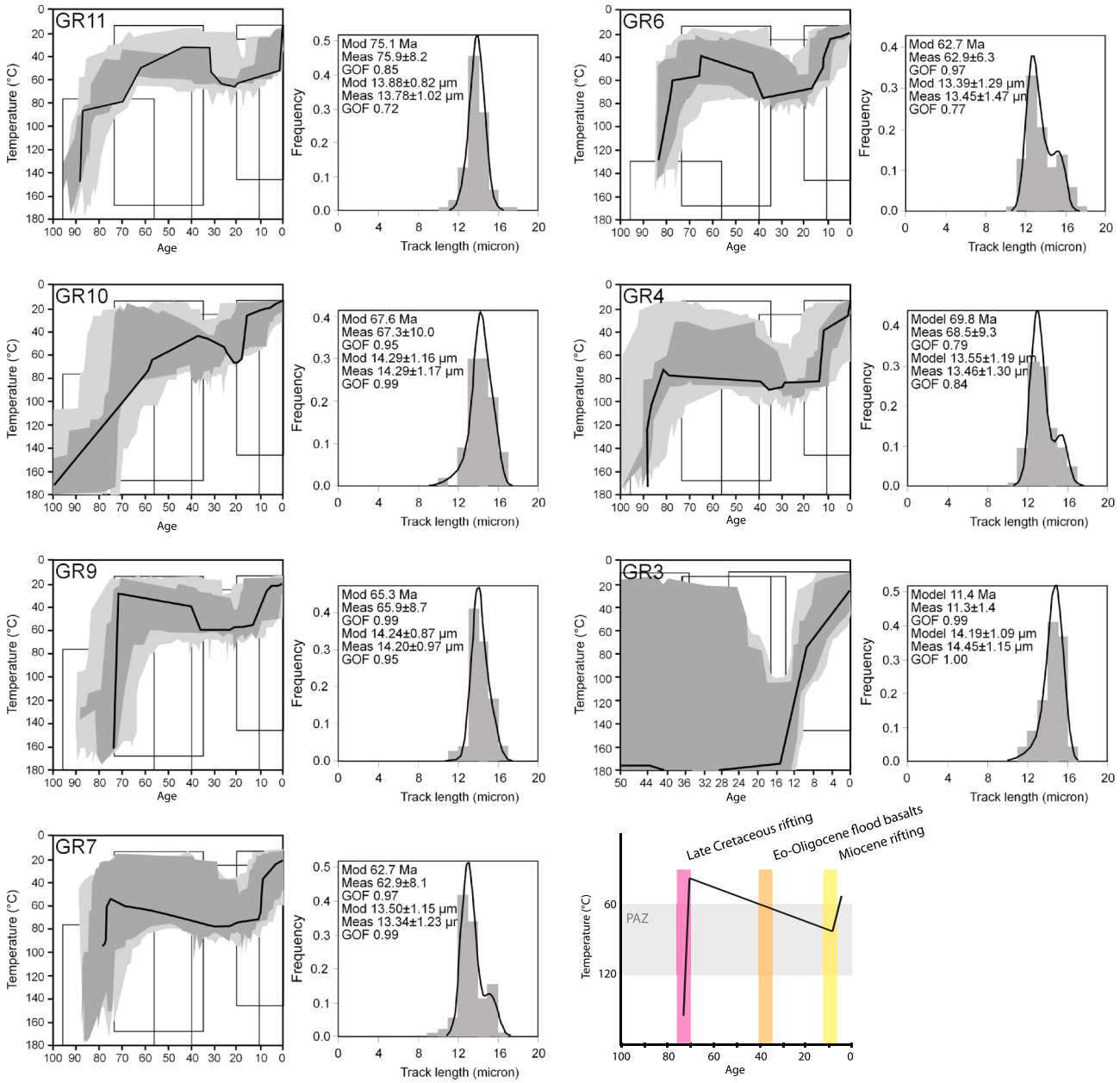

Figure 11. Thermal modeling of the AFT ages of the Beto basin (Gofa Province) performed with HeFTy program [*Ketcham et al.*, 2007b]. For each modeled sample, it shows (left) the T-t diagrams. The thick black lines indicate the best fitting paths. Dark gray envelopes stand for statistically good fit (statistical parameters are >0.50), whereas light gray envelopes stand for acceptable fit (statistical parameters are >0.05). (right) The modeled and measured age and track lengths for the best fitting path for each sample. The fission track lengths have been normalized for track angle using *c* axis projection [*Ketcham et al.*, 2007a, 2009], and the model used for annealing is from *Ketcham et al.* [2007b]. An interpretative cartoon showing the main steps of the exhumation history of the Gofa Province basement is also shown.

"Stream Profiler," a tool for geographic information system and MATLAB (available at: http://geomorphtools.org) developed by *Wobus et al.* [2006] and *Whipple et al.* [2007]. In log-log diagrams of slope versus area data, the concavity and steepness indices are the slope and *y* intercept of a regression line, respectively. Since θ and k_s are auto correlated, we normalized the steepness index (k_{sn}) by a reference concavity $\theta_{ref} = 0.45$ [e.g., *Wobus et al.*, 2006]. This allows the comparison of river longitudinal profiles, despite the widely varying drainage area. In addition, to investigate the general variation in steepness index values, we extracted the k_{sn} throughout the studied basins (Figure 13).

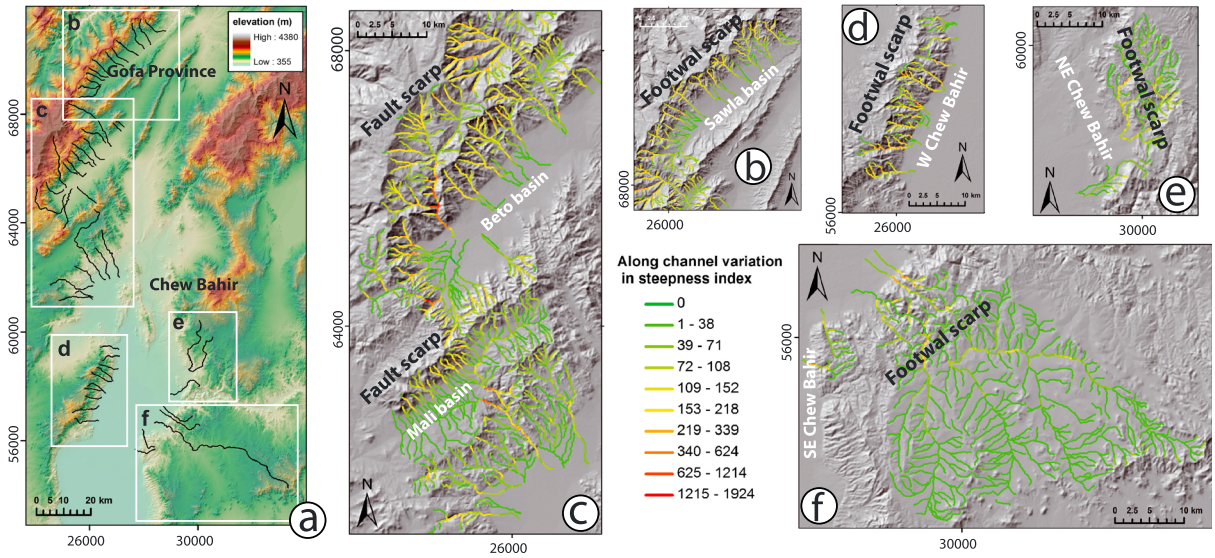

Figure 12. (a) SRTM DEM of the western sector of sMER showing the location of the Sawla, Beto, Mali, and Chew Bahir basins and of the studied rivers; (b–f) maps displaying the along channel variation in the steepness index in the studied drainages: warm colors indicate increase in k_{sn} values, locally corresponding with faults bordering the basins.

6.1. Sawla Basin

In the NE-SW trending Sawla basin, the axial river is located along the southeastern margin, although it becomes more central to the south (Figure 12b). The footwall scarp shows dissected facets and is drained by relatively small catchments. In the hanging wall, close to the fault scarp, the fans that constitute the piedmont are inactive and actively incised by rivers. The longitudinal profiles of rivers that drain the footwall have a smooth concave-up shape. Only few of them, especially in the southernmost portion of the basin, present a major knickpoint in correspondence with the main fault and minor knickpoints upstream. These profiles are characterized by high concavity (around 0.7) and values of steepness between 103 and 141 (Figure 13 and Table 5). The variation in steepness index along the channel shows generally a sudden increase in correspondence with the fault scarp.

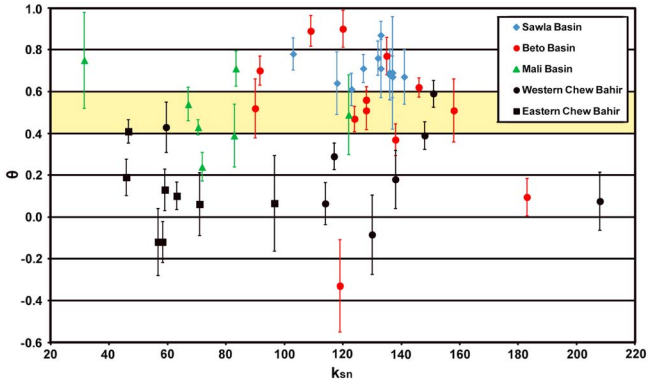

Figure 13. The θ versus k_{sn} diagram shows the variation in the river profile indices in the studied basins. The yellow band indicates the theoretical value range of concavity typical of a river in equilibrium. Many of the studied river profiles have highly irregular shapes, restraining them to be modeled properly. As a consequence, the uncertainty in concavity calculation is sometimes very high, as evidenced by the error bars. Despite this problem, the diagram shows a general progressive decrease in concavity from north (Sawla and Beto basins) to south (Mali and Chew Bahir basins). A parallel decrease characterizes the steepness index with the exception of the rivers draining the western Chew Bahir margin.

6.2. Beto Basin

In the NE-SW trending Beto basin, the axial river flows roughly in the center of the basin floor, where an evidence of change of courses and marshes are present (Figure 12c). The facets on the fault scarp are less incised than in the Sawla basin. Rivers do not incise the alluvial fans in the piedmont; moreover, there is a little evidence of recent fluvial activity. With respect to the Sawla basin river profiles, the Beto basin river profiles have, in general, a less smoothed shape, presenting wide knickzones, knickpoints, and rectilinear segments. The value range of both concavity and steepness indices increases (Figure 13 and Table 5) with respect to the rivers draining the Sawla basin, whereas the variation in channel slope along the channel point to

Table 5. Geomorphological Data: Concavity and Steepness Indices for Each Analyzed Stream of Figure 12a

River Numbering	Concavity Index (θ)	Normalized Steepness Index (k_{sn})
1	0.69 ± 0.086	136
2	0.67 ± 0.13	141
3	0.64 ± 0.15	118
4	0.71 ± 0.14	133
5	0.69 ± 0.27	137
6	0.61 ± 0.077	123
7	0.71 ± 0.068	127
8	0.76 ± 0.082	132
9	0.67 ± 0.1	137
10	0.78 ± 0.078	103
11	0.87 ± 0.067	133
12	0.68 ± 0.12	136
13	0.7 ± 0.07	91.6
14	0.89 ± 0.074	109
15	−0.33 ± 0.22	119
16	0.51 ± 0.15	158
17	0.095 ± 0.089	183
18	0.37 ± 0.076	138
19	0.77 ± 0.09	136
20	0.51 ± 0.092	128
21	0.47 ± 0.062	124
22	0.9 ± 0.069	120
23	0.56 ± 0.062	128
24	0.62 ± 0.045	146
25[a]	0.68 ± 0.15	0
26	0.52 ± 0.14	90
27	0.49 ± 0.19	122
28	0.75 ± 0.23	31.5
29	0.39 ± 0.15	82.8
30	0.71 ± 0.084	83.4
31	0.24 ± 0.068	71.6
32	0.54 ± 0.08	67.1
33	0.43 ± 0.037	70.5
34	0.43 ± 0.12	59.5
35[a]	0.29 ± 0.12	0
36	−0.085 ± 0.19	130
37	0.29 ± 0.063	117
38[a]	0.68 ± 0.081	0
39	0.064 ± 0.1	114
40	0.18 ± 0.14	138
41	0.39 ± 0.066	148
42	0.075 ± 0.14	208
43	0.59 ± 0.063	151
44	−0.12 ± 0.16	56.8
45	0.19 ± 0.088	45.9
46	−0.12 ± 0.099	58.3
47	0.061 ± 0.15	71
48	0.065 ± 0.23	96.6
49	0.41 ± 0.056	46.6
50	0.13 ± 0.1	59.1
51	0.1 ± 0.066	63.2

[a]Rivers not included in the diagram of Figure 13, since their profiles were impossible to be modeled, resulting in a $k_{sn} = 0$.

knickpoints located in correspondence of the NE-SW and NW-SE trending faults that border the basin to the NW (Figure 12c).

6.3. Mali Basin

At the northernmost edge of the Chew Bahir, the western margin of the Mali basin shows poorly incised facets and a less degraded footwall scarp (Figure 12c). The hanging wall of the fault consists of actively aggrading alluvial fans that form the piedmont. The longitudinal profiles of rivers that drain the footwall of the SW-NE fault are, in general, very irregular, some have a concave-up shape, but most of them are almost rectilinear. Indeed, they are less concave and less steep than the river profiles of Sawla and Beto basins (Figure 13). They are also characterized by knickzones and knickpoints, some located in correspondence of the main fault, as evidenced by the variation of channel steepness (Figure 13).

6.4. Chew Bahir Basin

The western margin of the Chew Bahir basin is a fault scarp characterized by well preserved facets, especially to the north, and by an aggradational alluvial fan (Figure 12d). In the eastern margin, the fault scarp is more incised, and wide progradational telescopic fans form a much wider piedmont (Figures 12e and 12f). The longitudinal profiles of rivers that drain the basin margins have a very irregular shape with many knickpoints and knickzones. There are strong variations in channel gradient, where the high values of steepness index correspond with the basin fault (Figure 13). Generally, the profiles are less concave than the river profiles of aforedescribed basins. Locally, the rivers on the western margin are steeper than the rivers on the eastern margin (Figure 13).

The analysis of hydrography, morphometry, and landforms in the Sawla, Beto, Mali, and northern Chew Bahir basins provides a general picture of the spatial variation in the interaction between erosion and tectonics. To the north, morphometric data and landforms indicate that the erosion rates overcame and counterbalanced tectonic rates in the Sawla and Beto basins, suggesting that the faults are either no longer active or have low extension rates in these areas. On the contrary, southward (i.e., Mali basin), the fresh landforms in both footwall and hanging wall, as well as the river longitudinal profiles indicate that landscapes are still far from responding to tectonic activity.

More south, in the Chew Bahir basin, data point to an even younger tectonic activity. The longitudinal profiles of rivers that drain the basement rocks on both basin margins show relatively very low concavity, indicating that hydrography is in a transient state of disequilibrium, possibly in response to tectonic activity. Along the western margin, the values of k_{sn} are higher (between around 110 and 210) than the ones relative to the rivers in the eastern margin (between around 40 and 100) (Figure 13). The higher values, observed in the western margin, could be interpreted as due to the footwall uplift of the active faults that bound the basin and keep the riverheads at higher elevation. A more recent fault activity and/or a higher tectonic rate are also confirmed by the fresh landforms. In particular, taking into account, that fans are very sensitive to variation in sediment supply and flood power related to climate; the western aggradational fans, where deposition occurs at the fan head, might result from higher tectonic rates than the eastern progradational fans, where deposition is downfan and fanheads are entrenched [*Keller*, 1986; *Harvey*, 2002; *Viseras et al*., 2003].

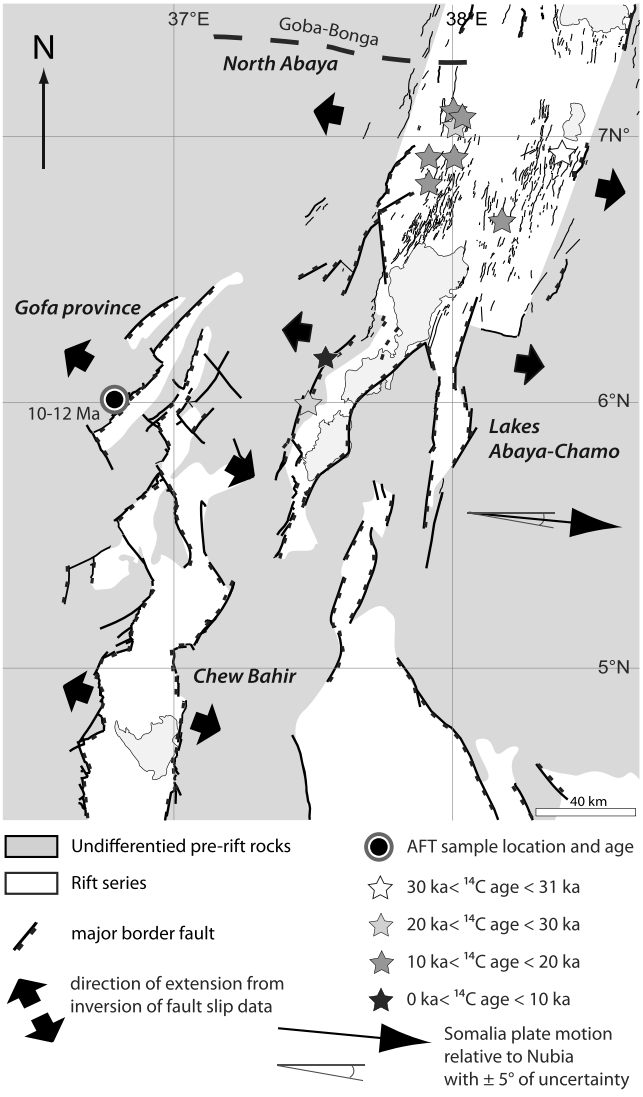

Figure 14. Scheme of the principal results of our study of the MER in southern Ethiopia. Thick black arrows indicate the kinematics of the four sectors of MER cropping out in southern Ethiopia. AFT dating of the basement exhumation in the Gofa Province is indicated by the gray/white dot. The stars indicate radiocarbon dating along the eastern and western margin.

In summary, morphometric data as well as basin landforms suggest that there is a spatial and probably temporal variation in tectonic activity in the sector extending from the Sawla basin to the northern Chew Bahir (Figure 12). To the north, the landscape is more close to an equilibrium state with respect to tectonic activity, whereas going to the south, it becomes more and more in disequilibrium, suggesting a southward younging of tectonic activity.

7. Discussion

7.1. Timing and Spatial Distribution of Deformation in Southern Ethiopia

Our new radiocarbon dating indicates a late Pleistocene-Holocene fault activities (post 30 ka; Figure 3 and Table 3) at both the western and eastern margins of the sMER (Figure 14). This shows that axial deformation is subordinate in this rift sector, in agreement with previous radiocarbon dating [*Corti et al*., 2013a], analysis of historical and recent seismicity [*Gouin*, 1979; *Keir et al*., 2006], morphotectonic investigations [*Boccaletti et al*., 1998], as well as recent GPS data [*Kogan et al*., 2012] suggesting active deformation along the margins of the sMER. At regional scale, it supports that an along axis, north to south decrease in rift maturity in the MER as a transition from axial tectonomagmatic deformation in the nMER to marginal deformation in the cMER and sMER is observed [e.g., *Hayward and Ebinger*, 1996; *Corti*, 2009].

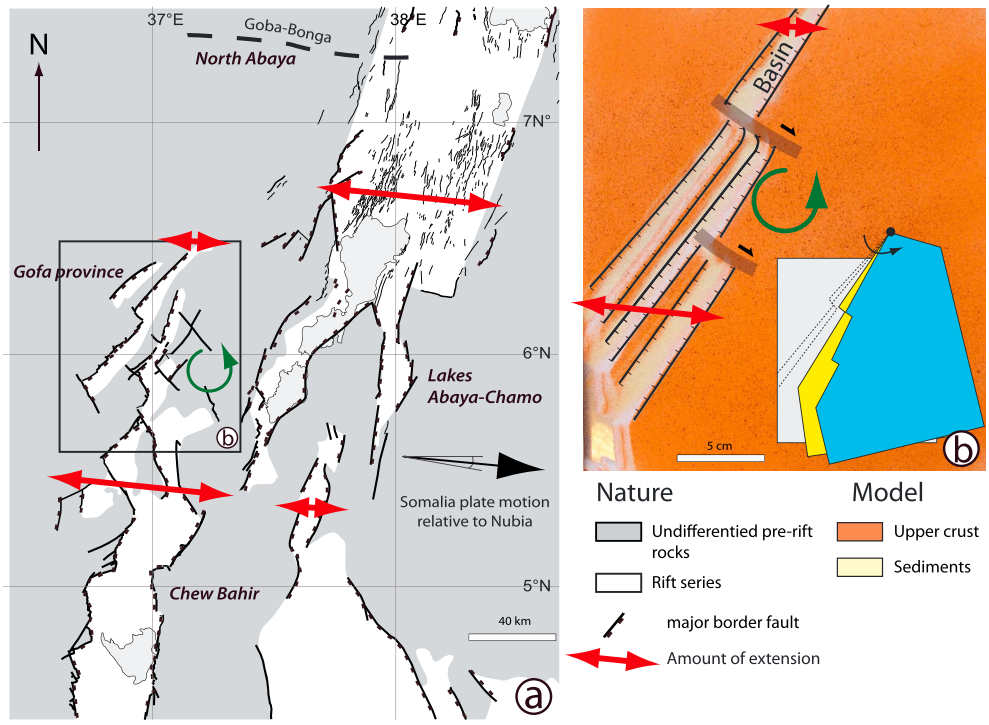

Figure 15. (a) Schematic map showing the across strike variations of extension within the MER and the Gofa province at the latitude of (i) Lake Abaya, where most of the extension is accommodated by the MER, and there is few to no extension in the Gofa province, and (ii) south of the Beto basin, where most of the extension is accommodated in the Gofa Province, and there is few to no extension in the MER. (b) Simple analog model illustrating the opening of the Gofa Province with a southward increasing of the amount of extension, resulting in large-scale counter clockwise rotation.

Although no radiocarbon dating is available for both the Gofa Province and the Chew Bahir, our geomorphological analysis suggests recent fault activity along the western margin of these basins. Coupled with the strong seismicity that characterizes the area, which is mostly associated with slip on border faults, these new data support previous models suggesting that the Kenyan rift and the MER are currently linked across a 200 km wide zone between the Omo and Segen basins [*Ebinger et al*., 2000]. Our analysis supports a decrease in ongoing fault activity to the north in the Gofa Province, in line with previous inferences by *Ebinger et al*. [2000]. This is also consistent with the current tectonic quiescence of the northernmost basins in the area (Omo Canyon, Mele) as suggested by *Wolde-Gabriel and Aronson* [1987]. Overall, this indicates a southward decrease in the amount of extension accommodated by the MER and a parallel increase in extension in the Gofa Province (Figure 15a). In this context, the majority of deformation is accommodated in the MER at the latitude of Lake Abaya, with only minor deformation in the Gofa Province. To the south, extension is mostly accommodated within the subparallel basins of the Gofa Province, and a more limited deformation occurs in the MER. Simple analog models support this view and indicate that the triangular shape—i.e., northward narrowing of the basins composing the Gofa Province—may be controlled by the local, southward increase in the amount of extension, a pattern that predicts large-scale counterclockwise rotations (Figure 15b; for further details on the analog modeling, we refer to the supporting information).

The new AFT data from the Gofa Province suggest that exhumation and fault development likely began at about 10–12 Ma (Figure 14), in line with previous geological findings from the Maze and Omo Canyon basins to the north [*Wolde-Gabriel and Aronson*, 1987]. Reported ages of basement exhumation are around 20 ± 2 Ma (AFT and U/Th-He on apatite [*Pik et al*., 2008]) in the Chew Bahir and point to an early Miocene activation of border faults in the area. In accordance with *Bonini et al*. [2005], this may support a northward propagation of the Kenyan rift-related extension in the area.

7.2. Style of Deformation and Influence of Preexisting Structures

The pattern of deformation highlights a substantial change in distribution of deformation, which varies from the single, narrow (80–100 km wide) rift valley in the cMER-nMER to a ~200 km wide belt of basins and ranges in the BRZ. This change has been related to both the north-south propagation of the two initially distinct MER and Kenyan rift systems and the eastward migration of deformation in the Turkana depression [*Ebinger et al*., 2000], the latter being likely controlled by strain hardening between the episodes of extension [*Morley et al*., 1992]. However, the widening of the area of active deformation corresponds to a significant crustal thinning between the MER (and surrounding plateaus) and the Turkana depression, related to the presence of preexisting Mesozoic NW-SE striking grabens (e.g., Anza graben). This indicates an important control exerted by both rheological changes and preexisting structures on the distribution of deformation in southern Ethiopia. These observations are in accordance with previous analog models [*Benes and Davy*, 1996; *Corti*, 2005] and theoretical studies [*e.g., Ebinger et al*., 2000] investigating the control of preexisting structures on the pattern of continental rifts, which suggest that extension in the presence of a thin crust is accommodated by a higher number of small faults and narrower basins with respect to areas with thicker crust. Accordingly, the reduced crustal thickness related to the preexisting Anza graben is responsible for a more diffuse deformation in southern Ethiopia.

Additionally, our data underline that preexisting basement fabrics govern the geometry of major border faults, an aspect particularly evident in the Gofa Province and Chew Bahir basin. In both areas, the border faults are highly segmented with different fault segments showing sharp changes in orientation related to the reactivation of two orthogonal main basement fabrics [e.g., *Corti*, 2009]. The simple analog models support this control and indicate the development of dextral transfer zones at basement-controlled offsets of major boundary faults (Figure 15).

7.3. Rift Kinematics

The inversion of fault slip data reveals that the overall extension directions trend ~N100–113°E and ~N123°E in the sMER-Chew Bahir sectors and Gofa Province, respectively (Figure 14). These results broadly agree with the available focal mechanism solutions (Figure 2). The overall ~N105°E trending extension direction computed on the whole fault population of the sMER is consistent with previous structural studies [*Corti et al*., 2013b]. Local variations in the paleostress field likely resulted from stress reorientations and/or influence of volcanic activity [e.g., *Acocella et al*., 2011]. The results in this area are strikingly similar to recent GPS data [*Kogan et al*., 2012], which also indicate a current N100°E directed extension at the latitude of Chencha (~6°N) (Figure 14).

To the south, the reconstructed extension direction varies from ~N123° in the Gofa Province to ~N113° in the Chew Bahir area. Slip along the border faults occurs mostly orthogonal to the main fault strike, indicating a pure extensional faulting in these basins (Figure 14). Notably, the basin axes in the Gofa Province as well as the trend of several fault segments in Chew Bahir basin are oblique to the Nubia-Somalia motion (Figure 14). This suggests that the computed extension directions for the three main sectors may not correspond to the actual Nubia-Somalia kinematics. Rotation of the extension direction resulting in pure dip-slip faulting at oblique rift margins has been indeed observed in other portions of the EARS (e.g., nMER and cMER [*Agostini et al*., 2011]; Western Branch [*Morley*, 2010]; and Gulf of Aden [*Bellahsen et al*., 2013]) and has also been described in other oblique rifts controlled by preexisting structures, such as the Baïkal rift [*Petit et al*., 1996]. This phenomenon has been attributed to local refraction of the extension direction at the margins of deep-seated, preexisting weaknesses oblique to the plate divergence during rift initiation [*Corti et al*., 2013b, and references therein]. In these areas, indeed, the principal strain directions are generally not parallel to the direction of plate motion but trend halfway between the plate divergence vector and the normal to the rift trend [*Withjack and Jamison*, 1986]. Alternatively, variations in buoyancy forces during rifting and thinning have also been shown to influence the stress pattern, leading to local rotation of extensional stresses at rift margins [*Bellahsen et al*., 2013, and references therein].

8. Conclusions

The new structural (fault kinematics), geochronological (^{14}C dating of fault gouges and apatite fission tracks), and geomorphological (fault scarps plus slope-area analysis) data provide new constraints on the timing, distribution, and characteristics of extensional deformation in southern Ethiopia. The main outcomes of this study are the following:

1. New radiocarbon dating indicates late Pleistocene-Holocene fault activities (post 30 Ka) at both western and eastern sMER margins; together with a limited axial deformation, this supports an along axis, north to south decrease in rift maturity in the MER.
2. New AFT data indicate exhumation and fault development in the Gofa Province at about 10–12 Ma, which may reflect a northward propagation of Kenyan rift-related deformation. After a period of quiescence, tectonic activity in southern Ethiopia was then resumed in the last 5 Ma, with renewed activity of large border faults and scattered volcanism.
3. Geomorphological analysis (integrated with the analysis of the local seismicity and previous geological data) suggests recent fault activity along the western margin of the various basins within the Gofa Province and the Chew Bahir, but a decrease in recent fault activity in the northern Gofa Province. This agrees with a model in which the Eastern and Main Ethiopian rifts are currently linked across a 200 km wide zone of ongoing tectonic activity.
4. Preexisting basement fabrics exert an important control on the geometry of major border faults, particularly in the Gofa Province and Chew Bahir basin, where the rift-related fault developed parallel to the basement fabrics.
5. Inversion of fault slip data indicates both regional and local variations of the extension direction. At a regional scale, the direction of extension strikes ~N100°E in the sMER, ~N113°E in the Chew Bahir basin, and N123°E in the Gofa Province. This behavior is likely dictated by the presence of deep-seated, preexisting weaknesses oblique to the plate divergence, as observed in other portions of the EARS. At a more local scale, variations of fault orientation are expected to control the computed direction of extension.

Acknowledgments

Tsegaye Abebe, Eugenio Carminati, Ameha Atnafu, and Asfaw Erbello are thanked for their discussions and support during fieldwork. M. Philippon, D. Sokoutis, E. Willingshofer, and M. Bonini acknowledge the financial support from the Marie Curie Initial Training Network TOPOMOD project 264517. M. Bonini, G. Corti, and F. Sani acknowledge the support from MIUR funds (PRIN2009-prot.2009H37M59). M. Bonini also acknowledges the support from CNR funds (RSTL 105 "Evoluzione della parte Nord del rift Afroarabico e distribuzione regionale delle georisorse"). Nicolas Bellahsen and an anonymous reviewer are thanked for their constructive comments, which greatly improve the paper. Onno Oncken and Claudio Faccenna are warmly thanked for the editorial handling.

References

Abbate, E., and M. Sagri (1980), Volcanites of the Ethiopian and Somalian Plateaus and major tectonic lines, *Atti Conv. Lincei*, *47*, 219–227.

Abebe, T., F. Mazzarini, F. Innocenti, and P. Manetti (1998), The Yerer–Tullu Wellel volcanotectonic lineament: A transtentional structure in Central Ethiopia and the associated magmatic activity, *J. Afr. Earth Sci.*, *26*, 135–150.

Abebe, T., P. Manetti, M. Bonini, G. Corti, F. Innocenti, F. Mazzarini, and Z. Pecksay (2005), Geological map (scale 1:200.000) of the northern main Ethiopian rift and its implication for the volcano-tectonic evolution of the rift *Maps and Charts series, MCH094*, 1 sheet, 20 text, Geol. Soc. of Am.

Abraham, A. (1989), Tectonic history of the pan-african low grade belt of western Ethiopia, *Ethiopian Institute of Geological Survey*, note 305, 22 pp.

Acocella, V., B. Abebe, and T. Korme (2011), Holocene opening directions along the axes of the Red Sea (Afar) and main Ethiopian rift: An overview, in *Volcanism and Evolution of the African Lithosphere*, Spec. Pap., vol. 478, edited by L. Beccaluva, G. Bianchini, and M. Wilson, pp. 25–35, Geol. Soc. Am., Boulder.

Agostini, A., M. Bonini, G. Corti, F. Sani, and P. Manetti (2011), Distribution of Quaternary deformation in the central main Ethiopian rift, East Africa, *Tectonics*, *30*, TC4010, doi:10.1029/2010TC002833.

Allmendinger, R. W., N. C. Cardozo, and D. Fisher (2011), *Structural Geology Algorithms: Vectors & Tensors*, 302 pp., Cambridge Univ. Press, Cambridge, doi:10.1017/CBO9780511920202.

Angelier, J. (1979), Determination of the mean principal direction of stress for a given fault population, *Tectonophysics*, *56*, T17–T26.

Angelier, J., and P. Mechler (1977), Sur une méthode graphique de recherche des contraintes principales également utilisable en tectonique et en sismologie: La méthode des dièdres droist, *Bull. Soc. Geol. Fr.*, *19*, 1309–1318.

Asfaw, L. M. (1990), Implication of shear deformation and earthquake distribution in the east African rift between 4N and 6N, *J. Afr. Earth Sci.*, *10*, 745–751.

Ayele, A., and R. Arvidsson (1998), Fault mechanisms and tectonic implication of the 1985–1987 earthquacke sequence in south-western Ethiopia, *J. Seismol.*, *1*, 383–394.

Bastow, I. D., D. Keir, and E. Daly (2011), The Ethiopia Afar Geoscientific Lithosphere Experiement (EAGLE): Probing the transition from continental rifting to incipient seafloor sreading, in *Volcanism and Evolution of the African Lithosphere*, Spec. Pap., vol. 478, edited by L. Beccaluva, G. Blanchini, and M. Wilson, pp. 1–26, Geol. Soc. Am., Boulder.

Bellahsen, N., L. Husson, J. Autin, S. Leroy, and E. d'Acremont (2013), The effect of thermal weakening and buoyancy forces on rift localization: Field evidences from the Gulf of Aden oblique rifting, *Tectonophysics*, *607*, 80–97.

Benes, V., and P. Davy (1996), Modes of Continental Lithospheric Extension: Experimental verification of Strain Localization Processes, *Tectonophysics*, *254*, 69–87, doi:10.1016/0040-1951(95)00076-3.

Benoit, M. B., A. A. Nyblade, and M. E. Pasyanos (2006), Crustal thinning between the Ethiopian and East African Plateaus from modeling Rayleigh wave dispersion, *Geophys. Res. Lett.*, *33*, L13301, doi:10.1029/2006GL025687.

Bhandari, N., S. C. Bhat, D. Lal, G. Rajagoplan, A. S. Tamhane, and V. S. Venka-Tavaradan (1971), Fission fragment tracks in apatite: Recordable track lengths, *Earth Planet. Sci. Lett.*, *13*, 191–199.

Boccaletti, M., M. Bonini, R. Mazzuoli, B. Abebe, L. Piccardi, and L. Tortorici (1998), Quaternary oblique extensional tectonics in the Ethiopian Rift (Horn of Africa), *Tectonophysics*, *287*, 97–116.

Bonini, M., G. Corti, F. Innocenti, P. Manetti, F. Mazzarini, T. Abebe, and Z. Pecskay (2005), Evolution of the Main Ethiopian Rift in the frame of Afar and Kenya rifts propagation, *Tectonics*, *24*, TC1007, doi:10.1029/2004TC001680.

Buck, W. R. (1991), Modes of continental lithospheric extension, *J. Geophys. Res.*, *96*, 20,161–20,178.

Buck, W. R. (2004), Consequences of asthenospheric variability on continental rifting, in *Rheology and Deformation of the Lithosphere at Continental Margins*, edited by G. D. Kamer et al., pp. 1–30, Columbia Univ. Press, New York.

Cardozo, N., and R. W. Allmendinger (2013), Spherical projections with OSXStereonet, *Comput. Geosci.*, *51*, 193–205, doi:10.1016/j.cageo.2012.07.021.

Claesson, S., J. S. Pallister, and M. Tatsumoto (1984), Samarium-Neodymium data on two late Proterozoïc ophiolites of Saudi Arabia and implications for crustal and mantle evolution, *Contrib. Mineral. Petrol.*, *85*, 244–252.
Corti, G. (2005), Dynamics of periodic instabilities during stretching of the continental lithosphere: View from centrifuge models and comparison with natural examples, *Tectonics*, *24*, TC2008, doi:10.1029/2004TC001739.
Corti, G. (2009), Continental rift evolution: From rift initiation to incipient break-up in the Main Ethiopian rift, East Africa, *Earth Sci. Rev.*, *96*, 1–53.
Corti, G., F. Sani, M. Philippon, D. Sokoutis, E. Willingshofer, and P. Molin (2013a), Quaternary volcano-tectonic activity in the Soddo region, western margin of the southern Main Ethiopian Rift, *Tectonics*, *32*, 861–879, doi:10.1002/tect.20052.
Corti, G., M. Philippon, F. Sani, D. Keir, and T. Kidane (2013b), Re-orientation of the extension direction and pure extensional faulting at oblique rift margins: Comparison between the Main Ethiopian Rift and laboratory experiments, *Terra Nova*, *25*, 396–404, doi:10.1111/ter.12049.
Davidson, A. (1983), The Omo River project, reconnaissance geology and Geochemistry of part of Illubabor, Kefa, Genu Gofa and Sidamo, *Ethiop. Inst. Geol. Surv, Minist. Mines Energy*, *2*, 1–89.
Delvaux, D., and B. Sperner (2003), Stress tensor inversion from fault kinematic indicators and focal mechanism data: The WinTENSOR program, in *New Insights into Structural Interpretation and Modelling*, Spec. Publ., vol. 212, edited by D. Nieuwland, pp. 75–100, Geol. Soc. London, London.
Dunkl, I. (2002), Trackkey: A windows program for calculation and graphical presentation of fission-track data, *Comput. Geosci.*, *28*, 3–12.
Ebinger, C. J. (2005), Continental breakup: The East African perspective, *Astron. Geophys.*, *46*, 2–21.
Ebinger, C. J., T. Yemane, G. Woldegabriel, J. L. Aronson, and R. C. Walter (1993), Late Eocene-recent volcanism in the southern main Ethiopian rift, *J. Geol. Soc. London*, *150*, 99–108.
Ebinger, C. J., T. Yemane, D. J. Harding, S. Tesfaye, S. Kelley, and D. C. Rex (2000), Rift deflection, migration, and propagation: Linkage of the Ethiopian and Eastern rifts, Africa, *Geol. Soc. Am. Bull.*, *112*, 163–176.
Fernandes, R. M. S., B. A. C. Ambrosius, R. Noomen, L. Bastos, L. Combinck, J. M. Miranda, and W. Spakman (2004), Angular velocities of Nubia and Somalia from continuous GPS data: Implications on present-day relative kinematics, *Earth Planet. Sci. Lett.*, *222*, 197–208.
Flint, J. J. (1974), Stream gradient as a function of order, magnitude, and discharge, *Water Resour. Res.*, *10*, 969–973.
Foster, A. N., and J. A. Jackson (1998), Source parameters of large African earthquakes: Implications for crustal rheology and regional kinematics, *Geophys. J. Int.*, *134*, 422–448.
Foster, D. A., and A. J. W. Gleadow (1996), Structural framework and denudation history of the flanks of the Kenya and Anza rifts: East Africa, *Tectonics*, *15*, 258–271.
Galbraith, R. F. (1981), On statistical models of fission track count, *Math. Geol.*, *13*, 471–488.
Gallagher, K. (1995), Evolving temperature histories from apatite fission-track, *Earth Planet. Sci. Lett.*, *136*, 421–435.
Gouin, P. (1979), *Earthquakes History of Ethiopia and the Horn of Africa*, 258 pp., IRDC, Ottawa.
Green, P. F., and I. R. Duddy (1989), Some comments on paleotemperature estimation from apatite fission tracks analysis, *J. Pet. Geol.*, *12*, 111–114.
Guiraud, R., W. Bosworth, J. Thierry, and A. Delplanque (2005), Phanerozoic geological evolution of northern and central Africa: An overview, *J. Afr. Earth Sci.*, *43*, 83–143.
Hack, J. T. (1957), Studies of longitudinal profiles in Virginia and Maryland, *U.S. Geol. Surv. Prof. Pap.*, *294*(B), 45–97.
Harvey, A. M. (2002), Effective timescales of coupling within fluvial systems, *Geomorphology*, *44*, 175–201.
Hayward, N. J., and C. Ebinger (1996), Variations in the along-axis segmentation of the Afar rift system, *Tectonics*, *15*, 244–257.
Hoke, G. D., B. L. Isacks, T. E. Jordan, N. Blanco, A. J. Tomlinson, and J. Ramezani (2007), Geomorphic evidence for post-10 Ma uplift of the western flank of the central Andes 18°30′–22°S, *Tectonics*, *26*, TC5021, doi:10.1029/2006TC002082.
Howard, A. D., W. E. Dietrich, and M. A. Seidl (1994), Modeling fluvial erosion on regional to continental scales, *J. Geophys. Res.*, *99*, 13,971–13,986.
Hurford, A. J. (1990), Standardization of fission track dating calibration: Recommendation by the Fission Track Working Group of the I.U.G.S. Sub commission on Geochronology, *Chem. Geol.*, *80*, 171–178.
Kazmin, V., A. Shifferaw, and T. Balcha (1978), The Ethiopian basement: Stratigraphy and possible manner of evolution, *Geol. Rundsch.*, *67*, 531–546.
Keir, D., C. J. Ebinger, G. W. Stuart, E. Daly, and A. Ayele (2006), Strain accommodation by magmatism and faulting as rifting proceeds to breakup: Seismicity of the northern Ethiopian rift, *J. Geophys. Res.*, *111*, B05314, doi:10.1029/2005JB003748.
Keir, D., I. D. Bastow, C. Pagli, and E. L. Chambers (2013), The development of extension and magmatism in the Red Sea rift of Afar, *Tectonophysics*, *607*, 98–114.
Keller, E. A. (1986), Investigations of active tectonics: Use of surficial earth processes, in *Active Tectonics*, pp. 136–147, National Academy Press, Washington, D. C.
Keranen, K., and S. L. Klemperer (2008), Discontinuous and diachronous evolution of the Main Ethiopian Rift: Implications for the development of continental rifts, *Earth Planet. Sci. Lett.*, *265*, 96–111.
Keranen, K., S. L. Klemperer, R. Gloaguen, and the EAGLE working group (2004), Three-dimensional seismic imaging of a protoridge axis in the Main Ethiopian rift, *Geology*, *32*, 949–952.
Keranen, K., S. L. Klemperer, J. Julia, J. L. Lawrence, and A. Nyblade (2009), Low lower-crustal velocity across Ethiopia: Is the Main Ethiopian Rift a narrow rift in a hot craton?, *Geochem. Geophys. Geosyst.*, *10*, Q0AB01, doi:10.1029/2008GC002293.
Ketcham, R. A. (2005), Forward and Inverse Modeling of Low-Temperature Thermochronometry Data, *Rev. Mineral. Geochem.*, *58*, 275–314.
Ketcham, R. A., R. A. Donelick, and M. B. Donelick (2000), AFTSolve: A program for multikinetic modeling of apatite fission-track data, *Geol. Mater. Res.*, *2*, 1–32.
Ketcham, R. A., A. C. Carter, R. A. Donelick, J. Barbarand, and A. J. Hurford (2007a), Improved measurement of fission-track annealing in apatite using c-axis projection, *Am. Mineral.*, *92*, 789–798.
Ketcham, R. A., A. C. Carter, R. A. Donelick, J. Barbarand, and A. J. Hurford (2007b), Improved modeling of fission-track annealing in apatite, *Am. Mineral.*, *92*, 799–810.
Ketcham, R. A., R. A. Donelick, M. L. Balestrieri, and M. Zattin (2009), Reproducibility of apatite fission-track length data and thermal history reconstruction, *Earth Planet. Sci. Lett.*, *284*, 504–515.
Kirby, E., and K. X. Whipple (2001), Quantifying differential rock-uplift rates via stream profile analysis, *Geology*, *29*, 415–418.
Kirby, E., C. Johnson, K. Furlong, and A. Heimsath (2007), Transient channel incision along Bolinas Ridge, California: Evidence for differential rock uplift adjacent to the San Andreas fault, *J. Geophys. Res.*, *112*, F03S07, doi:10.1029/2006JF000559.

Kogan, L., S. Fisseha, R. Bendick, R. Reilinger, S. McClusky, R. King, and T. Solomon (2012), Lithospheric strength and strain localization in continental extension from observations of the East African Rift, *J. Geophys. Res.*, *117*, B03402, doi:10.1029/2011JB008516.
Kroner, A., W. Todt, I. M. Hussein, M. Mansour, and A. A. Rashwan (1992), Dating of late Proterozoic ophiolites in Egypt and the Sudan using the single grain zircon evaporation technique, *Precambrian Res.*, *59*, 15–32.
Levitte, D., J. Columba, and P. Mohr (1974), Reconnaissance geology of the Amaro horst, southern Ethiopian rift, *Geol. Soc. Am. Bull.*, *85*, 417–422.
Mengesha, T., Tadiwos, C., and H. Workineh (1996), *Geological map of Ethiopia*, 2nd ed., Bulletin of the Ethiopian Institute of Geological Survey, *3*, scale 1:2.000.000, 1 sheet. OCLC: 46451457, Addis Abeba.
Mohr, P., and B. Zanettin (1988), The Ethiopian flood basalt province, in *Continental Flood Basalts*, Petrology and Structural Geology, vol. 3, edited by J. D. Macdougall, pp. 63–110, Dordrecht.
Moore, J. M., and A. Davidson (1978), Rift structure in southern Ethiopia, *Tectonophysics*, *46*, 159–173.
Morley, C. K. (2010), Stress re-orientation along zones of weak fabrics in rifts: An explanation for pure extension in 'oblique' rift segments?, *Earth Planet. Sci. Lett.*, *297*, 667–673.
Morley, C. K., W. A. Wescott, D. M. Stone, R. M. Harper, S. T. Wigger, and F. M. Karanja (1992), Tectonic evolution of the northern Kenya rift, *J. Geol. Soc. London*, *149*, 333–348.
Pallister, J. S., J. S. Stacey, L. B. Fischer, and W. R. Premo (1988), Precambrian ophiolites of Arabia: Geologic settings, U-Pn geochronology, Pb-isotope characteristics, and implications for continental accretion, *Precambrian Res.*, *38*, 1–54.
Petit, C., J. Déverchére, F. Houdry, V. A. Sankov, V. I. Melnikova, and D. Delvaux (1996), Present-day stress field changes along the Baikal rift and tectonic implications, *Tectonics*, *15*, 1171–1191.
Pik, R., B. Marty, J. Carignan, G. Yirgu, and T. Ayalew (2008), Timing of East African Rift development in southern Ethiopia: Implication for mantle plume activity and evolution of topography, *Geology*, *36*, 167–170.
Schoenbohm, L. M., K. X. Whipple, B. C. Burchfiel, and L. Chen (2004), Geomorphic constraints on surface uplift, exhumation, and plateau growth in the Red River region, Yunnan Province, China, *Geol. Soc. Am. Bull.*, *116*, 895–909, doi:10.1130/B25364.1.
Snyder, N., K. X. Whipple, G. E. Tucker, and D. J. Merritts (2000), Landscape response to tectonic forcing: Digital elevation model analysis of stream profiles in the Mendocino triple junction region, northern California, *Geol. Soc. Am. Bull.*, *112*(8), 1250–1263.
Spiegel, C., B. P. Kohn, D. X. Belton, and A. J. Gleadow (2007), Morphotectonic evolution of the central Kenya rift flanks: Implications for late Cenozoic environmental change in East Africa, *Geology*, *35*, 427–430.
Stamps, D. S., E. Calais, E. Saria, C. Hartnady, J. M. Nocquet, C. J. Ebinger, and R. M. Fernandes (2008), A kinematic model for the East African Rift, *Geophys. Res. Lett.*, *35*, L05304, doi:10.1029/2007GL032781.
Stern, R. J. (1994), Arc assembly and continental collision in the Neoproterozoic East African orogeny, *Annu. Rev. Earth Planet. Sci.*, *22*, 319–351.
Stern, R. J. (2002), Crustal evolution in the East African Orogen: A neodymium isotopic perspective, *J. Afr. Earth Sci.*, *34*, 109–117.
Tarboton, D. G., R. L. Bras, and I. Rodriguez-Iturbe (1989), Scaling and elevation in river networks, *Water Resour. Res.*, *25*, 2037–2051.
Thybo, H., and C. A. Nielsen (2009), Magma-compensated crustal thinning in continental rift zones, *Nature*, *457*, 873–876.
Viseras, C., M. L. Calvache, J. M. Soria, and J. Fernández (2003), Differential features of alluvial fans controlled by tectonic or eustatic accommodation space. Examples from the Betic Cordillera, Spain, *Geomorphology*, *50*, 181–202.
Whipple, K. X. (2001), Fluvial landscape response time: How plausible is steady state denudation?, *Am. J. Sci.*, *301*, 313–325, doi:10.2475/ajs.301.4-5.313.
Whipple, K. X. (2004), Bedrock rivers and the geomorphology of active orogens, *Annu. Rev. Earth Planet. Sci.*, *32*, 151–185.
Whipple, K. X., and G. E. Tucker (1999), Dynamics of the stream-power river incision model: Implications for height limits of mountain ranges, landscape response timescales, and research needs, *J. Geophys. Res.*, *104*, 17,661–17,674.
Whipple, K. X., C. Wobus, B. Crosby, E. Kirby, and D. Sheehan (2007), New Tools for Quantitative Geomorphology: Extraction and Interpretation of Stream Profiles from Digital Topographic Data, Geol. Soc. of Am. Annual Meeting, Short Course Guide, Denver. [Available at http://www.geomorphtools.org.]
White, R. S., L. K. Smith, A. W. Roberts, P. A. F. Christie, N. J. Kusznir, and The iSIMM Team (2008), Lower-crustal intrusion on the North Atlantic continental margin, *Nature*, *452*, 460–464.
Willgoose, G., R. L. Bras, and I. Rodriguez-Iturbe (1991), A coupled channel network growth and hillslope evolution model: I. Theory, *Water Resour. Res.*, *27*, 1671–1684.
Withjack, M. O., and W. R. Jamison (1986), Deformation produced by oblique rifting, *Tectonophysics*, *126*, 99–124.
Wobus, C., K. X. Whipple, E. Kirby, N. Snyder, J. Johnson, K. Spyropolou, B. Crosby, and D. Sheehan (2006), Tectonics from topography: Procedures, promise, and pitfalls, in *Tectonics, Climate, and Landscape Evolution*, Spec. Pap., vol. 398, edited by S. Willett et al., pp. 55–74, Geol. Soc. Am, Boulder.
Wolde-Gabriel, G., and L. Aronson (1987), Chow Bahir rift: A "failed" rift in southern Ethiopia, *Geology*, *15*, 430–433.
Wolde-Gabriel, G., T. Yemane, T. White, B. Asfaw, and G. Suwa (1991), Age of volcanism and fossils in the Burji-SOyoma area, Amaro horst, southern main Ethiopian rift, *J. Afr. Earth Sci.*, *13*, 437–447.
Wolfenden, E., C. Ebinger, G. Yirgu, A. Deino, and D. Ayale (2004), Evolution of the northern main Ethiopian rift: Birth of a magmatic margin, *Earth Planet. Sci. Lett.*, *224*, 213–228.
Ziegler, P. A., and S. Cloetingh (2004), Dynamic processes controlling evolution of rifted basins, *Earth Sci. Rev.*, *64*, 1–50.